Large-scale infra-slow dynamics of extracellular potentials linked to synchronous states revealed by graphene neural probes

Garcia-Cortadella, R.[1,2], Cisneros-Fernandez, J.[3], Schwesig, G.[1], Shahidi, A.[1], Umurzakova, A.[1], Schäfer, N.[2], Aguilar, J.[3], Masvidal-Codina, E.[2,3], Del Corro, E.[2], Moahrlok, R.[4], Kurnoth, M.[4], Paetzold, J.[4], Loeffler, H.[4], Jeschke, C.[4], Meents, J.[4], Illa, X.[3], Serra-Graells, F.[3], Guimerà-Brunet, A.[3], Garrido, J. A.[2,5], Sirota, A.[1]**

1. Bernstein Center for Computational Neuroscience Munich, Faculty of Medicine, Ludwig-Maximilians Universität München, Planegg-Martinsried, Germany
2. Catalan Institute of Nanoscience and Nanotechnology (ICN2), CSIC and BIST, Campus UAB, Bellaterra, 08193, Barcelona, Spain
3. Centro de Investigación Biomédica en Red en Bioingeniería, Biomateriales y Nanomedicina (CIBER-BBN), Madrid, Spain
4. Multi Channel Systems MCS GmbH, Reutlingen, Germany
5. ICREA, Pg. Lluís Companys 23, 08010, Barcelona, Spain

* Corresponding authors

Abstract

Brain states exhibit slow transitions that are coordinated by slowly varying homeostatic and neuromodulatory factors. These slow dynamics modulate neuronal excitability, giving rise to brain state-specific synchronous oscillatory patterns across brain regions. Such synchronous states could be reflected in local infra-slow variations in the extracellular potential, providing new insights into the organisation of spontaneous brain dynamics beyond the established fast time scales. However, mapping of the LFP across brain regions with high spatio-temporal resolution remains challenging, with the infra-slow component particularly elusive. To overcome these limitations, we developed neural probes based on arrays of up to 512 multiplexed graphene transistors, which enable DC-coupled, high-density, and large-scale recordings of surface and depth activity in freely behaving rats. Analysis of cortex-wide oscillation dynamics improves segmentation, provides new insights into global brain states and allows detection of the local oscillatory states. Brain state transitions related to changes in neuronal synchrony are found to correlate with topographically structured infra-slow dynamics. Furthermore, transregional infra-slow waves during non-REM sleep are globally coupled to diverse sleep spindle oscillatory modes independent of their localization while slow oscillations locally modulate spindle occurrence. This study shows that spatio-temporal patterns of infra-slow and slow LFP parallel the spatially organized oscillatory dynamics, reflecting the interplay between sub-cortical inputs and cortical excitability across brain states.

Introduction

Understanding how spontaneous brain dynamics emerge and evolve to structure behaviour is one of the central questions in neuroscience. The state of large-scale brain networks is shaped by a myriad of slowly varying physiological processes including neuromodulatory dynamics and homeostatic factors[1–5]. These variables modulate neuronal excitability and effective connectivity and therefore the emergent synchronous neuronal dynamics at various time scales from seconds to minutes. Infra-slow excitability fluctuations, related to the level of arousal, have been shown to shape brain state transitions[4,6–9], constraining complex spatiotemporal brain dynamics to a low-dimensional latent space[10–12]. In the context of pathological states, infra-slow local field potentials (LFP) have been related to hypersynchronous interictal epileptic events[13], showing the connection between infraslow dynamics and healthy brain function. These physiological and pathological patterns of infra-slow brain activity have been observed in terms of population activity changes[9,14], neuromodulatory dynamics[4,15,16], variations in oxygenation level[17,18] and fluctuations in membrane potential[19] or calcium concentration[20]. However, recording of infra-slow LFP has remained limited to spatially coarse measures[18,21–23].

Despite the potential role of infra-slow dynamics in coordinating brain-wide activity across spatio-temporal scales[6,9,19,20,24–27], current brain mapping technologies do not enable full-band mapping across large brain areas with submillimeter resolution. On the one hand, optical and magnetic imaging techniques present a limited temporal resolution and are often not suitable for chronic experiments in freely moving animals, which are required for the investigation of unconstrained brain states and behavioural dynamics. On the other hand, large-scale electrophysiological recordings are limited in their sensitivity at very low frequencies and in their spatial resolution across large areas. One potential approach to address this technical challenge is to upscale the number of channels in micro-ECoGs while enhancing their sensitivity in the infra-slow band. However, despite recent advances in high channel count flexible micro-electrocorticography (ECoG) arrays[28–33], no method has yet demonstrated DC-coupled LFP mapping across large cortical areas with high spatial resolution. Accomplishing this challenge could provide valuable insights into the role of infra-slow and slow brain activity in coordinating the fast synchronization between neuronal populations at different spatio-temporal scales[3,6,34], linking research in small animal models and non-invasive imaging studies in humans[7,24,27].

In this study, we leverage large-scale multiplexed graphene transistor arrays to overcome this central challenge in neuroimaging. Recent advances in graphene technology showed that graphene solution-gated field-effect transistors (g-SGFETs) are promising building blocks for high-channel-count neural probes. Previous studies showed the suitability of g-SGFETs for DC-coupled, chronic recordings in freely moving rodents[35–37] as well as their operation in multiplexed mode[38–40]. The combination of these key features is exploited in this study for large-scale and high spatio-temporal resolution mapping of DC-coupled signals in freely moving rats. We demonstrate brain mapping with high channel-count probes, up to 512 channels, chronically implanted in a cohort of animals. Furthermore, we demonstrate the seamless combination of multiplexed ECoGs with multiplexed depth graphene probes for the simultaneous recording of epi-cortical and intra-cortical DC-coupled LFP.

The spatio-temporal characteristics obtained through this approach reveal the relation between topographically structured and layer-dependent infra-slow dynamics and varying levels of neuronal synchronization related to physiological and pathological brain states. First, we perform brain state segmentation based on high dimensional spatio-spectral features. Then, we analyze the spatio-temporal infra-slow dynamics related to hypersynchronous spike-and-wave discharges and

sleep sub-state transitions. Finally, we present a detailed characterisation of sleep spindle oscillatory modes, uncovering a rich variety of generators globally coupled to infra-slow LFP and locally modulated by slow oscillations (SO). These results suggest that topographic and layer-specific neuronal synchronization, linked to sustained gradients in extracellular K^+ concentration[41,42], could lead to the generation of localized dipoles by the electrogenic NaK pumps. Our study opens the door to the use of multiplexed graphene probes for high spatio-temporal resolution neural interfaces with implications in clinical and fundamental neuroscience research, from the detection and manipulation of pathological states to the understanding of large-scale neuronal synchronization dynamics.

Results

Graphene-based active neural probes and dedicated recording systems

Graphene transistors operate as transducers, converting extracellular potentials into current variations between the drain and the source (Fig. 1a). This sensing mechanism, together with the graphene's electrochemical stability, enables high-quality DC-coupled recordings, avoiding amplifier saturation and minimizing drifts[36]. Furthermore, transistors can be arranged in addressable arrays, enabling the implementation of time-domain multiplexing[39,40]. Implementing the read-out circuitry at the output of the rows of the arrays and sequentially switching the drain-to-source bias across columns reduces the complexity of connectors and enables up-scaling the number of channels[40] (Fig. 1a).

Here, we demonstrate the use of custom-built electronics for the operation of high-count transistor arrays in freely moving rats. We show the operation of an open-source system with 256 channels for early adoption of the technology[40] (Methods and Supplementary Information S1), as well as a headstage based on an application-specific integrated circuit (ASIC)[38] to enhance the channel count scalability, reaching 512 channels in freely moving rats (Fig. 1a, Supplementary Information S1). In multiplexed operation, the graphene probes presented a median equivalent noise at the gate of 3.4µV (Q1= 2.8µV and Q3=6.0µV) per frequency decade (see Supplementary Information S2 for a detailed characterization). Furthermore, we demonstrated the embedding of addressable transistor arrays into narrow linear probes (Fig. 1b), integrating 32 channels in a 106µm wide probe consisting of 3 metal layers[35,43,44]. In this manner, ECoGs and depth probes could be seamlessly combined and operated with the same recording system (by sharing read-out blocks and sampling resources), enabling DC-coupled, dense recordings across cortical layers simultaneously with surface recordings.

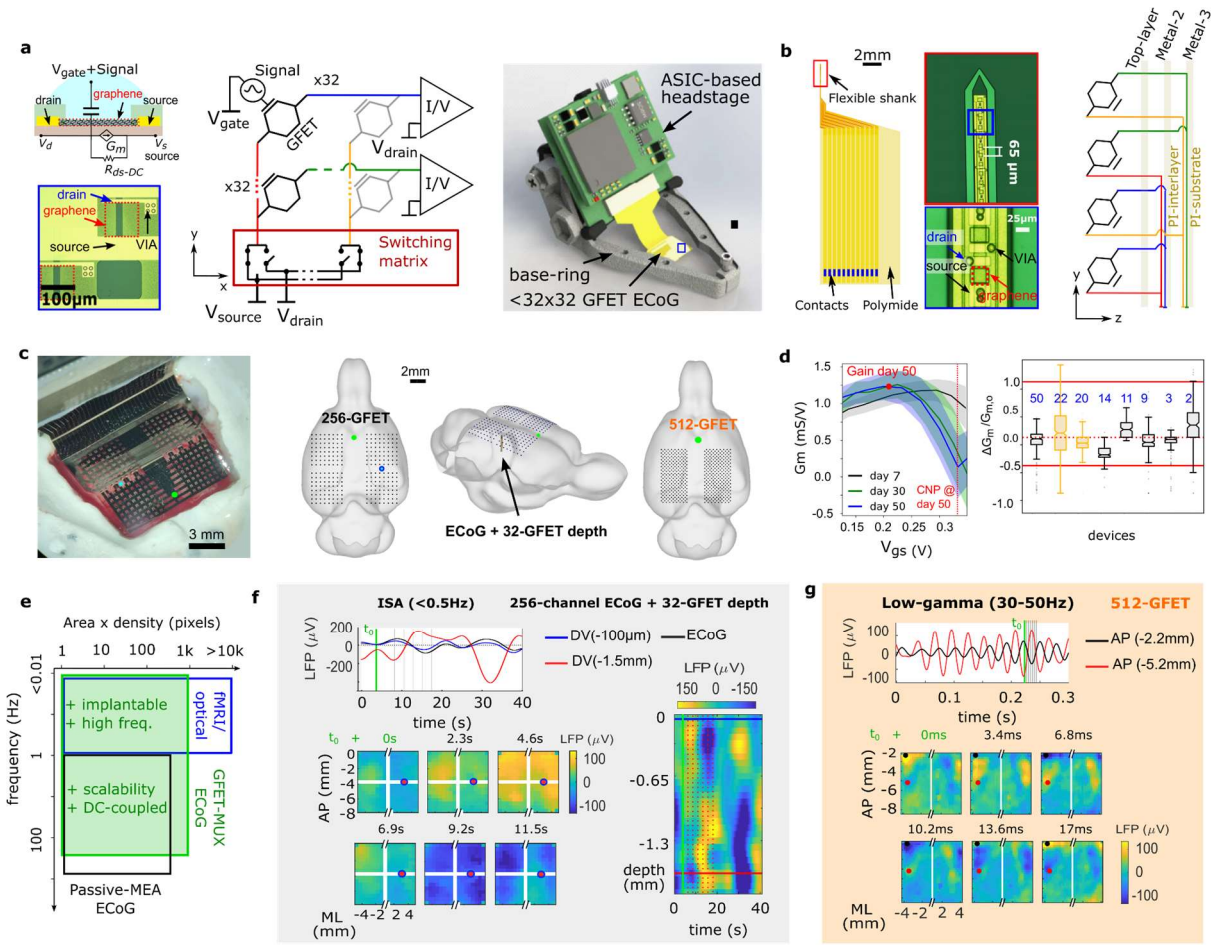

Figure 1| Graphene-based multiplexed large-scale recording technology. a. Schematic of a g-SGFET and its equivalent circuit (top-left). Optical micrography of the graphene transistor array with the position of drain, source, active graphene area and vertical-interconnect-access (VIA) connections indicated (bottom-left). Schematic of a multiplexed g-SGFET array, each hexagon represents a g-SGFET. Rows and columns are connected to the I-V converters and a switching matrix respectively (middle). The headstage and graphene neural probes are shown as assembled on a 3D-printed base ring for implantation (right). **b.** Layout of a 32-channels graphene depth probe (left). Optical micrograph showing the tip of the depth probe (middle). Schematic of a multiplexed g-SGFET array arranged in a linear probe, where multiple metal layers are used to reduce its width (right). **c.** Micrograph of a 256-channel g-SGFET ECoG array implanted over the neocortex of a rat (left) and schematics showing the position of the arrays. Blue dot, the position of the insertion of depth probes; green dot, Bregma (right). **d.** Left: Voltage-dependent transconductance (Gm): median (solid line) and standard deviation (transparent area) for all GFETs in a 256-channel ECoG. Right: the change in Gm from the first day to the last day (in blue) normalised by the Gm on day 1 for all functional GFETs in 256-channel (black) and 512-channel (orange) ECoGs. Red lines, two-fold increase/decrease of Gm. Blue numbers, the number of days implanted for each device (see supplementary Information S4). **e.** Schematic comparison of the spatio-temporal resolution of various imaging techniques. The advantages of multiplexed graphene probes compared to other techniques are indicated in green. **f.** Examples of traces in the infra-slow band (top-left) from representative ECoG and two intracortical channels. Infra-slow voltage maps recorded with a 256-channel ECoG (bottom-left). The white gaps indicate gaps between channel rows/columns (see panel c). The blue circle indicates the insertion point of the depth probe. Infra-slow LFP depth profile (right), where the blue and red lines indicate the channels corresponding to the traces on the left panel. **g.** Examples of traces in the low-gamma band (top), and low-gamma voltage maps recorded with a 512-channel ECoG (bottom). White space indicates the gap between hemispheres. The red and black dots indicate the channels corresponding to the two traces on top.

To explore the spatio-temporal dynamics of wide-band LFP during spontaneous behaviour with the improved sensing capabilities of graphene probes, we implanted large-scale ECoGs covering a large fraction of the dorsal neocortex in 8 rats (6 of them with 256-channel and 2 with 512-channel ECoGs, see Fig. 1c, Methods and Supplementary Information S3). Additionally, in a subset of animals, surface recordings were combined with multiplexed graphene depth probes (n=2, see Fig. 1c). Electrophysiological recordings were performed in combination with high-precision 3D motion capture of the rat's head for the classification of behavioural states in recording sessions lasting between 46 min and 248 min (mean of 145.8 min). The neural probes were chronically implanted, showing a stable sensitivity, quantified by transconductance (Gm) of transistors, for up to 50 days (see Fig. 1d and Supplementary Information S4). The large-area coverage and high spatio-temporal resolution measurement of the DC-coupled LFP enabled by these devices provided a unique imaging-like electrophysiological window into wide-band brain dynamics (Fig. 1e), as illustrated by the examples of spatio-temporal patterns in the infra-slow and gamma band in Fig. 1f,g and Movies 1 and 2.

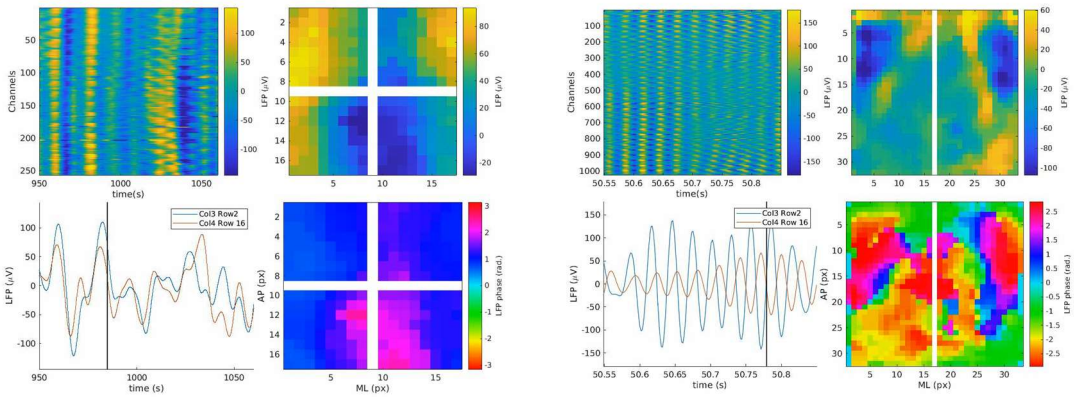

Movie 1 and 2| The movies of the infra-slow dynamics (256 channel ECoG, movie 1) and low-gamma band dynamics (512 channel ECoG, movie 2). Top left, color-coded voltage across channels and time; top right, maps of voltage. The bottom left panel shows the traces from two individual channels specified in the legend, running black line tracks the time of the frame shown in the top right. The bottom right panel shows the color-coded maps of the instantaneous phase of the LFP in the respective band. Note that time points and channels with low power show an uninterpretable phase.

High-dimensional spatio-spectral characterization of brain states

Similar to how high-density multichannel recordings at micro and meso-scales enable the detection and classification of single units and high-frequency oscillations based on their invariant spatial sources[45], macro-scale recordings could provide an insight into anatomical localization of the sources of the slow oscillatory LFP associated with global brain states. Indeed, the use of multiple channel recordings combined with spectral analysis improves brain state classification[46]. Leveraging on the topographic dense sampling of LFP over the entire dorsal neocortex, and indirectly sampling the dynamics of volume conducted sources localized in the underlying brain areas[47], we hypothesised that the spatial localization of the oscillatory dynamics sources could help with the identification and classification of brain states.

To characterise the variable topography of the oscillatory dynamics associated with distinct brain states, we first computed spectrograms of the LFP and integrated spectral power within various frequency bands for all channels, from delta to low-gamma (Supplementary Information S5). The spatio-spectral characteristics of global brain dynamics were then compressed into the first three

principal components, which were used for state classification based on a Gaussian mixture model (Fig. 2a). This approach compressed covarying spatio-spectral features and allowed their reliable identification of the three major electrophysiological states; slow-wave (SW) state, theta state and high-voltage spindles (HVS)[48–50]. The electrophysiological state segmentation was complemented with the motor state extracted from the 3D tracking data to subdivide behavioral-physiological states into slow-wave sleep (SWS), rapid eye movement (REM) sleep, awake non-theta (Aw. non-theta), awake theta, associated with active movement (THE) and micro-arousals (defined as short bouts of movement during SWS) (Fig. 2b and Methods).

Using the obtained labels of the data segments as ground truth, we tested the separability of data points in the full-dimensional spatio-spectral space without considering the motor information. The separability between state clusters was assessed by embedding spatio-spectral data into a 2-dimensional space using Uniform Manifold Approximation and Projection (UMAP) and computing cluster isolation metric (*L_ratio,* see Methods) in that space (Fig. 2c). The obtained *L_ratio* was then compared to the distribution of *L_ratio* obtained from UMAP-transformed features derived from individual channels treated independently (Fig. 2d). Indeed, separability of labelled states was substantially increased when taking into account spatio-spectral features for the classification, even leading to effective segregation of states that partially overlap in terms of spatial and spectral content, such as THE and REM. The improvement of cluster isolation metric when using the full dimensional spatio-spectral characteristics compared to independent channels was consistently present across animals for all the identified states (Fig. 2e, t-test confirms a significant reduction in *L_ratio* across animals and states).

Large-scale and dense mapping of brain activity also enabled the characterization of brain-state-specific spatio-spectral features across cortical regions (Fig. 2f), which contributed to their separability. The mean power maps in space and frequency revealed the spatio-spectral fingerprints of the identified states (Fig. 2g,h), which were consistent across animals (Fig. 2i). Specifically, theta power during THE and REM sleep had a broad peak roughly aligned with the projection of the hippocampus on the cortical surface (see atlas in Fig. 2g for reference), while the second harmonic of theta was maximal in the anterior locations (Supplementary Information S6). During THE state and REM sleep, the mean power profiles also presented a prominent peak in the low-gamma band (30-40 Hz) in anterior regions, overlaying motor and somatosensory areas (Fig. 2h). During SWS, the power in the delta band was maximal in central-anterior areas, with relatively large variability across animals (Supplementary Information S6), while the spindle power was stronger over somatosensory cortices (Fig. 2g-i). Finally, HVSs consistently presented a broadly distributed fundamental (7-10 Hz band) with multiple harmonics with increasingly prominent anterior localization for higher-order harmonics (Fig. 2g-i).

These results suggest that leveraging high-density multichannel recordings over the entire dorsal neocortex can significantly enhance the classification and characterization of brain states. In the following sections, spatio-spectral characteristics of brain states are used to study the topographical relation between oscillatory dynamics and infra-slow LFP.

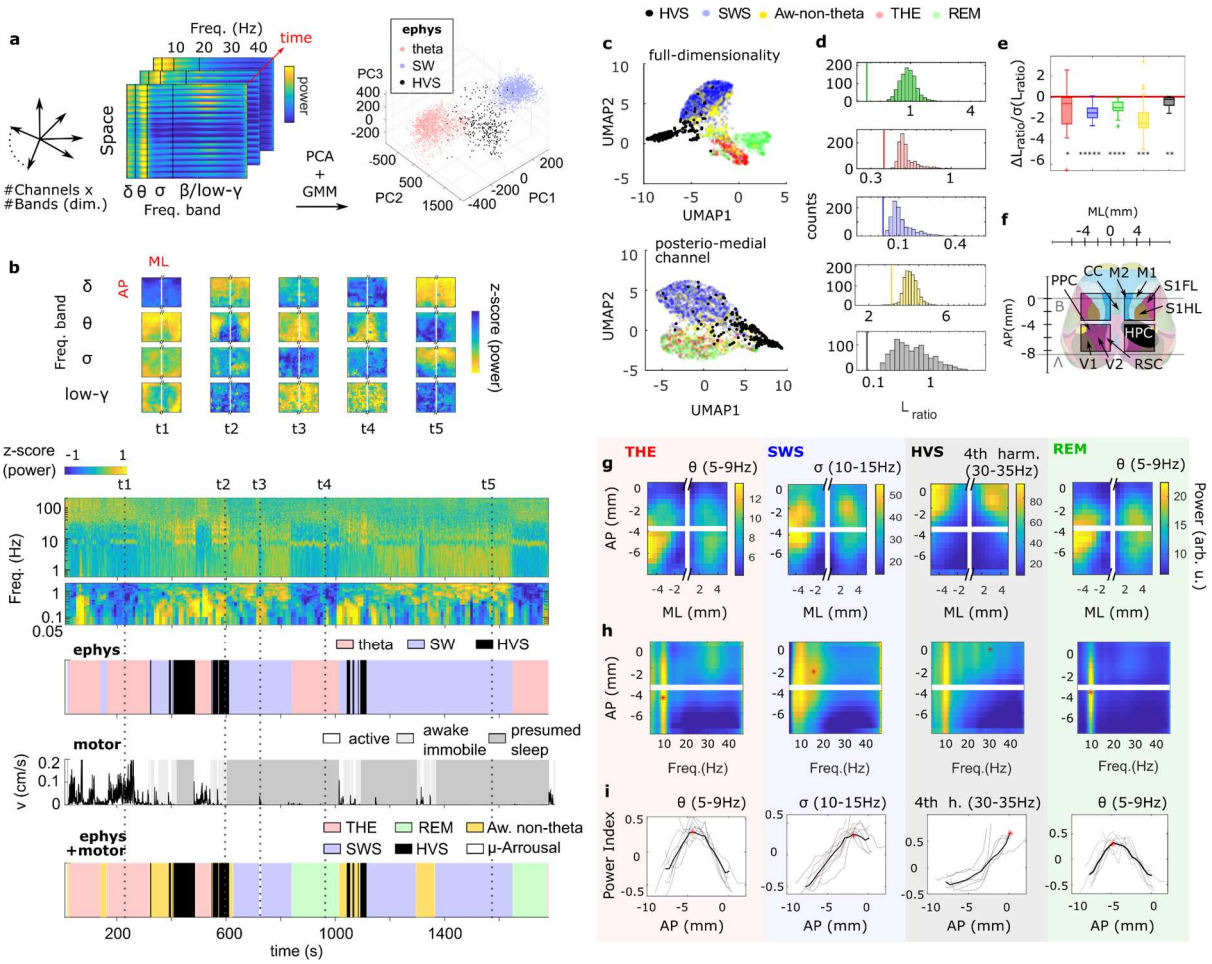

Figure 2| Spatio-spectral characteristics of brain states. a. Representation of the brain state classification procedure. Spectral content in various frequency bands in all channels is used as features for a classifier based on PCA and a GMM. **b.** From top to bottom: example frames of the power across frequency (rows) and time points (columns). Example spectrogram (z-scored) spanning from infra-slow (0.05Hz) to high-gamma (200Hz) bands. Resulting electrophysiological states. The motor state overlapped with the speed of the animal. Combination of the motor state with the electrophysiological state. **c.** UMAP embedding of spatio-spectral characteristics from all channels (top) and from an example posterior channel (bottom). **d.** Distribution of the *Lratio* extracted from individual channels across the array and *Lratio* from full-dimensionality spatio-spectral data (vertical line). **e.** Difference between the *Lratio* from full-dimensionality spatio-spectral data and the median of the *Lratio* distribution across channels (normalized by its standard deviation) (n=8 animals, one-tailed t-test p-values: *0.0019, **0.00017, ***1.1e-6, ****3.3e-9, *****4.9e-12). **f.** Atlas of the rat brain (obtained from EBRAINS database). Projection of the hippocampus on the surface in black. The non-shadowed area represents the sampled area by 256-channel ECoGs. **g.** Top: mean spectrum across the array for THE, SWS, HVS, and REM states (from left to right) within a certain frequency range (top labels). Middle: mean spectrum averaged across the mediolateral axis vs frequency for THE, SWS, HVS, and REM (from left to right). The mean spectrum has been re-whitened using an autoregressive model within each state. The red stars mark the peak in power for the frequency band shown in the top row. Bottom: Mean spectrum averaged across the medio-lateral axis within a certain frequency band (top labels), for the THE, SWS, HVS and REM (from left to right). Shaded lines correspond to different animals and the solid line is the mean (n=8 animals for THE, REM and SWS). For HVS, n=6 animals where this state was detected.

Spike and wave discharges drive local shifts in the DC extracellular potentials

Having characterised the spatio-spectral characteristics of prominent brain states we next evaluated their spatio-temporal infra-slow correlates across cortical regions. Firstly, we focused on the HVS state, which is a hypersynchronous thalamocortical oscillation that is considered a model of absence epilepsy[49,51] and has been previously linked to spatially inhomogeneous DC shifts[37] (with some works suggesting a non-pathological basis for this state[48–50]). Understanding the relation between this state of hypersynchronous neuronal firing and the DC potential shifts across brain regions and cortical layers could provide clues about the physiological origin of infra-slow LFP and guide the discovery of biomarkers for the detection of epileptic foci. Our main objective was to assess whether the high power in somatosensory areas for the broadband spike-and-wave discharges of HVS (Fig. 2g-i) is linked to matching infra-slow spatio-temporal dynamics and to explore the spatial and laminar profile of the DC shifts associated with this most synchronous thalamocortical oscillation.

To characterize the infra-slow correlates of HVS, we analysed the coactivation of infra-slow and spindle-band sources. The duration of HVS episodes showed a long-tailed distribution with a median of 4.7s Fig. 3a, Supplementary Information S7). The HVS events were associated with a striking DC-potential shift linked to the spike-and-wave activity (Fig. 3b), which had a larger amplitude in those areas where the power of spike-and-wave discharges was larger (Fig. 3c). To complement spatial characterisation we combined an ECoG with depth graphene probe implanted in one animal through an opening in the active ECoG into the somatosensory cortex (ML 3.2mm/ AP -3.4mm). The DC-potential shift reversed its polarity along the translaminar axis reaching maximal amplitude in deep cortical layers (Fig. 3c). To quantify this observation across all channels, the LFP around the HVS onset (-20s to +20s) was temporally decomposed into two bands by band-pass filtering in the 5-30Hz band or low-pass filtering below 0.5Hz. These two bands were spatially decomposed by independent component analysis (ICA) to identify potentially matching sources for DC-potential shifts and spike-and-wave discharges (Fig. 3d). The resulting independent components (IC) were sorted based on their RMS amplitude around the HVS onset and the cross-correlation between the HVS-onset and peaks in the activation dynamics (Fig. 3e, f and Methods). The IC-relevance index (see Methods) dropped quickly for higher ICs, indicating that both energy and temporal dynamics of the wide-band LFP associated with HVS are mostly described by the first component in both frequency bands (Fig. 3f and Supplementary Information S7). Inspection of the infra-slow IC1 reconstructed LFP and its spectrogram confirmed the correlation between infra-slow dynamics and spike-and-wave discharges for the first IC (Fig. 3g). The loadings of the first IC presented a consistent negative gradient across animals in the anterior to posterior, as well as in the lateral to medial directions (Fig. 3h, i). The depth profile of the HVS showed a phase reversal of the first IC around layer IV for DC-potential shifts as well as for the first IC of spike-and-wave discharges (see Fig. 3c, i). Overall, these results show that HVS, as hypersynchronous thalamocortical oscillation, generates not only localised spike-and-wave discharges but also a temporally aligned, topographically and trans-laminarly matching DC-potential shift.

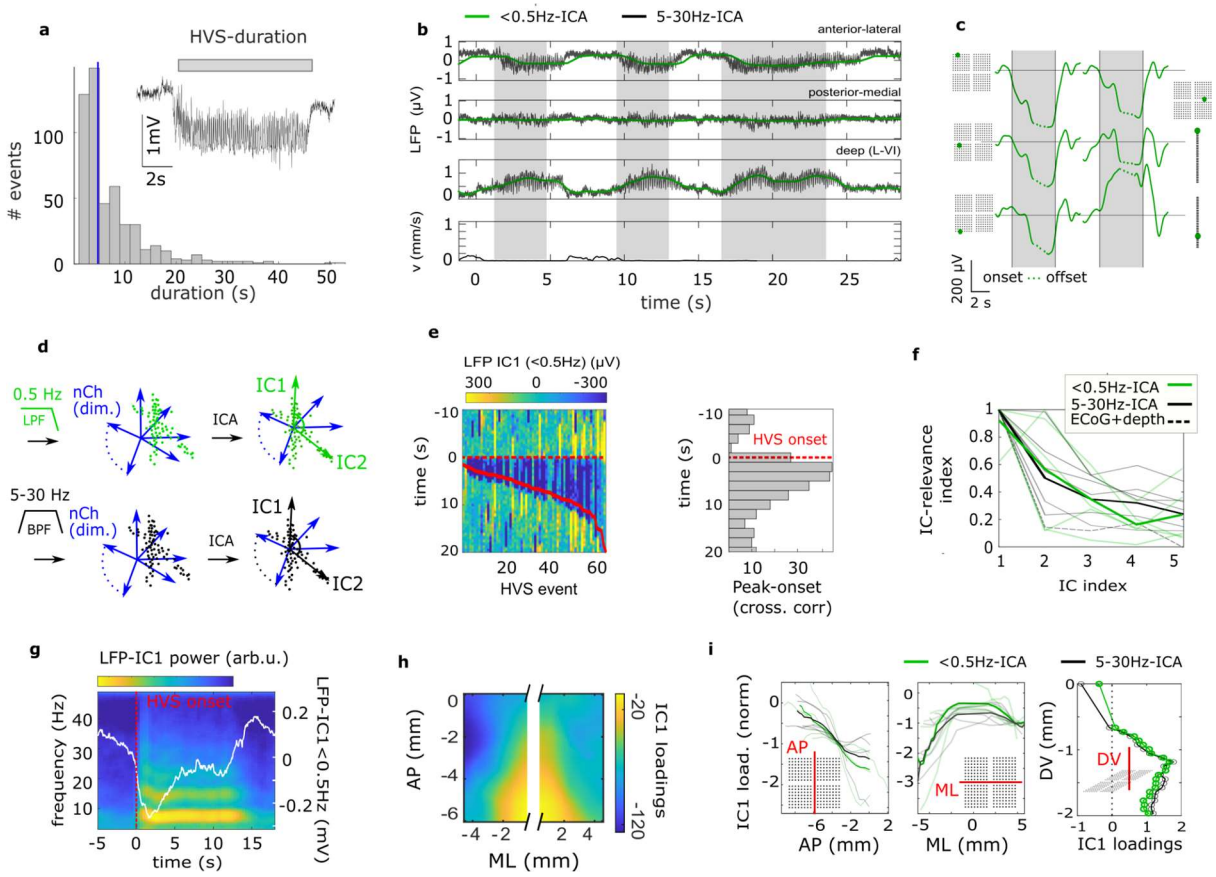

Figure 3| Topographic structure of infra-slow and spike-and-wave sources of high voltage spindles. a. Distribution of HVS duration across animals (median, blue line). The inset shows an example of full-band LFP during HVS. **b.** LFP during the occurrence of several HVS events (<30Hz, black and <0.5Hz, green). From top to bottom: LFP for representative anterior-lateral, posterior-medial and deep channels and speed of the animal. **c.** Mean infra-slow (<0.5Hz) LFP around the HVS onset and offset (red vertical lines) for various channels in AP (left) and DV (right) axes. **d.** LFP in the infra-slow and 5-30 Hz was decomposed by ICA separately. **e.** Colour-coded reconstructed LFP from the first IC (<0.5Hz) across HVS events (left) and cross-correlogram of the infra-slow peaks to the HVS onset (right). Red lines indicate state onset and offset. **f.** IC-relevance index for the first five ICs (see Methods, n=6 animals). **g.** The riggered average of the reconstructed LFP spectrogram around the HVS onset overlaid with the triggered average of the infra-slow reconstructed LFP for the 1st IC. **h.** Median loadings of the first IC across animals (n=6 animals). **i.** Comparison of the first IC loadings across animals (n=6 animals) in the three axes (thick line shows the mean across animals). IC loadings were normalized by their value at -3.5mm w.r.t. Bregma in the AP axis, 4mm w.r.t. the midline in the ML axis and at -1mm w.r.t. the surface for the DV axis.

Infra-slow LFP dynamics mark the transition between arousal levels

We posited that as HVS, an exceptionally synchronous state, is associated with infra-slow dynamics, transitions in and out of synchronous slow wave sleep would likely be also marked by infra-slow dynamics. Indeed, recent studies have explored the relationship between the level of arousal and the microstructure of sleep sub-states[52,53,54]. During SWS, the power of sleep spindles varies at the infra-slow time scale, marking cycles in sleep fragility[53] linked to neuromodulatory dynamics[4,5,26,55]. Similarly, neuromodulatory infra-slow dynamics promote the transition into REM sleep[4,5]. Despite recent progress, the infra-slow LFP correlates of these neuromodulatory and thalamocortical synchronisation dynamics, as well as their relation to the microstructure of sleep regulation, remain largely unexplored and limited to human EEG studies due to technical limitations[56].

To characterize the spatial structure of infra-slow LFP we performed singular value decomposition (SVD) of the LFP during the sleep epochs, including SWS, micro-arousals and REM-sleep and surrounding 10s epochs (Fig. 4a). SVD revealed that after removing global variations in the signal captured by the first SV component, the second SV component displayed an anterio-posterior and medio-lateral gradient that is topographically consistent across animals (Fig. 4b). Equivalently, inspecting the infra-slow content (<0.5 Hz) of the LFP after subtracting the contribution from the first SV component showed transient prominent fluctuations with opposite polarity for anterior and posterior channels (Fig. 4c). The troughs in the SV2 score that captured these events appeared to coincide with micro-arousals and REM epochs, suggesting a correlation between this component and the depth of sleep.

Temporal dynamics of these infra-slow LFP fluctuations, characterized by the inter-trough interval distribution within SWS, spanned time scales of 10 to 100 seconds with median being 50 seconds, which is significantly faster than median time scale of intervals between micro-arousals detected from motor activity, which were on the order of minutes (Fig. 4d). The cross-correlation of the detected troughs with the micro-arousal and the REM states onset confirmed their co-occurrence with the SVD-derived infra-slow fluctuations (Fig. 4e, top). Furthermore, the troughs in the posterior-anterior LFP gradient revealed subtle (subthreshold, <0.5mm/s) movements beyond overt micro-arousals with a significant correlation between the amount of movement and the arousal-related gradient amplitude (Spearman correlation r=0.22, p-value = 0.0017, see Supplementary Information S9). Further inspecting the relation between SV2 score dynamics and sleep sub-states, revealed the relation between the duration of SV2 score shifts and the duration of micro-arousals and REM sleep epochs (Fig. 4e, middle). To quantify this relationship, we calculated the duration of subthreshold SV2 scores following state transitions and assessed their rank correlation with state duration (Fig. 4e, bottom). Notably, REM sleep epochs exhibited qualitatively distinct infra-slow dynamics depending on their duration, with shorter (<1 min) and longer (>1 min) epochs reflecting a different covariance structure (Fig. 4e and Supplementary Information S10). Specifically, longer REM epochs showed no significant correlation between their duration and the duration of DC shifts in the SV2 score, indicating the emergence of infra-slow dynamics during long REM epochs. In contrast, shorter REM epochs and micro-arousals were significantly correlated to the duration of infra-slow LFP patterns, suggesting the occurrence of a DC-potential shift associated with the transition from SWS into more asynchronous states.

In order to interpret the polarity of the DC-potential shifts, the potential has to be referenced to a particular state. Referencing the LFP (<0.5Hz) to the micro-arousal and REM DC level reveals that the gradient captured by SV2 is associated with a negative DC shift in anterior-lateral areas during the SWS states that parallels the HVS case (Fig. 4f-h). Consistent with previous observations[53], spindle power showed a gradual and global increase preceding the micro-arousal and REM onsets across the array and an abrupt decline at the micro-arousal and REM onsets recovering to baseline at an infra-slow time scale (Fig. 4f-h and Supplementary Information S11). On the contrary, low gamma power showed a brief bout at the micro-arousal and REM onsets (Fig. 4f, h and Supplementary Information S11). The triggered average of the translaminar LFP around micro-arousals and REM-sleep epochs referenced to these states showed the phase reversal of the DC potential around L-IV (Fig. 4i, j). Similarly to the signal on the surface, the duration of DC-shift in depth corresponding to the inactive state correlates with the micro-arousal and REM epochs duration (rank correlation 2 animal r= [0.36, 0.33], p-value= [0.02, 0.018] for micro-arousals, and r= [0.74, 0.40], p-value= $[1.1\ 10^{-6}, 0.07]$ for REM, p-values computed from a t-distribution approximation, Fig. 4k). Taken together, these results show

that the infra-slow LFP presents topographical dynamics linked to sleep sub-states transitions, which parallels previously observed neuromodulatory, and thalamocortical synchronization dynamics.

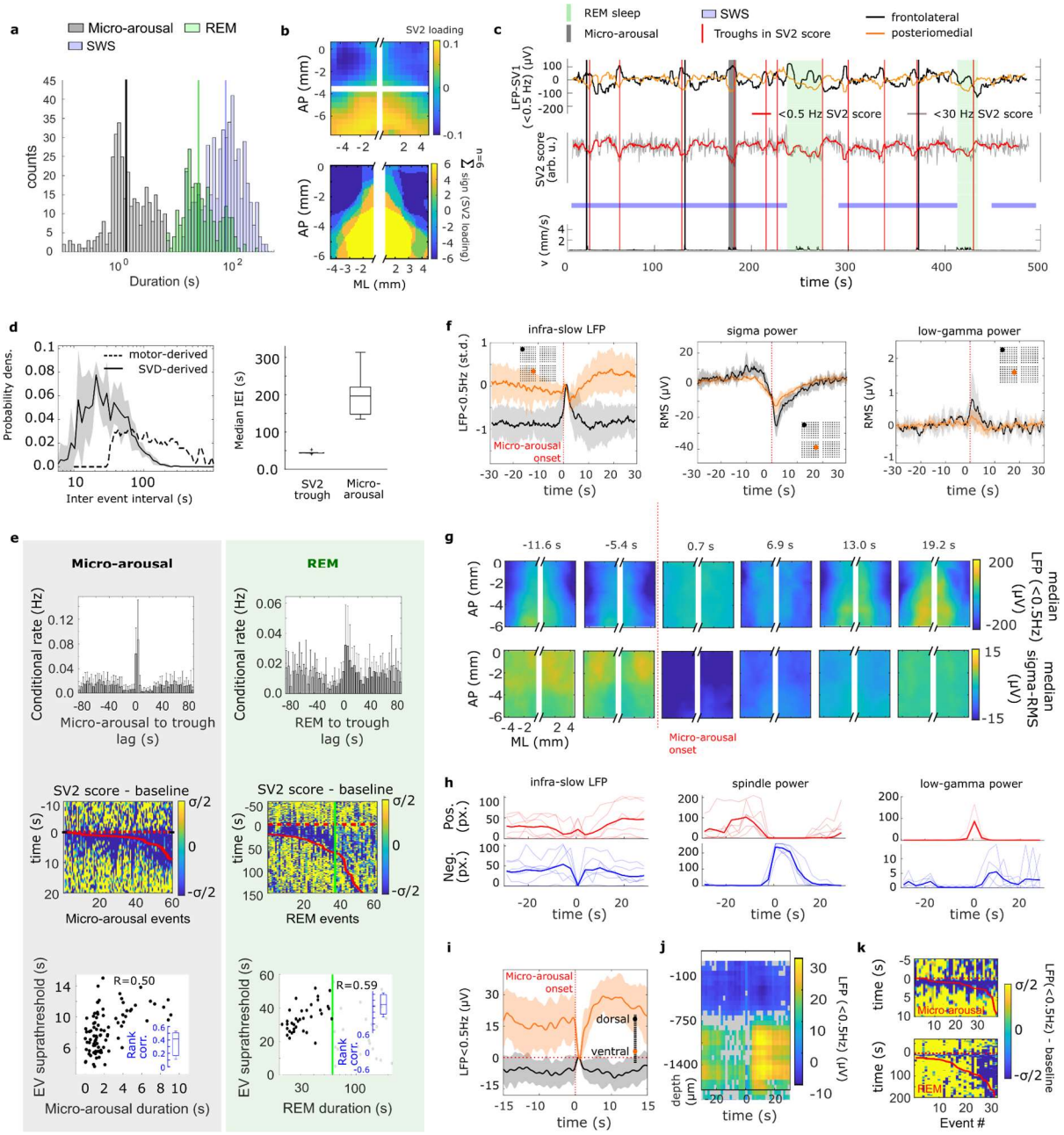

Figure 4| Infra-slow LFP correlates of sleep state transitions. a. Duration of detected REM sleep, SWS and micro-arousal epochs across animals. **b.** Coefficients of the second left-singular vector represented in space for an example animal (top) and the sum of the sign of the second singular vector across animals (n=6) represented in space (bottom). **c.** From top to bottom: LFP after subtracting the contribution from SV1 for two channels, score of the SV2 (<30Hz) and (<0.5Hz), brain states and velocity of the reflective markers on the animal head. Red lines, troughs of SV2 score. **d.** Left: distribution of inter-event intervals (IEI) between SV2 score troughs (90th percentile in prominence) during SWS (including micro-arousals), mean and standard deviation across animals (n=6) and the IEI distribution between micro-arousals accumulated across animals. Right: boxplot of median IEI for SV2 score troughs and micro-arousals across animals (n=6 animals). **e.** Characteristics of micro-arousal (left) and REM (right) states. Top: cross-correlation between state onsets and troughs in SV2 score (standard deviation shown as error bars, n=6 animals). Middle: colour-coded SV2 score around the state onsets across state events (sorted by duration) for an example animal (red lines indicate state onset and offset). Bottom: scatter plot of the state duration vs supra-threshold score suppression duration for an example animal (the inset shows the rank correlation across 6 animals). **f.** Triggered average of infra-slow LFP (left), spindle power (middle) and low-gamma power (right) on the micro-

arousal onset across animals (n=6). The thick lines correspond to the mean and the dashed area to the standard deviation. Insets show the position of coloured traces on the array. **g.** Median infra-slow (<0.5Hz) field potential (top) and sigma power (bottom) triggered average around the micro-arousal onset across animals (n=6). **h.** The number of pixels showing positive (top) and negative (bottom) variations significantly deviating from 0 (permutation test FDR-corrected p<0.05, 1000 permutations). From left to right: for infra-slow LFP, sigma power and low-gamma power. **i.** Triggered average of infra-slow LFP in depth for the superficial channel (DV = -100µm) in black and deep channel (DV = -1.1mm) in orange. Mean and standard deviation across events for an example animal. **j.** Mean LFP, as in panel i, across the depth profile. Grey pixels represent non-significant deviations from 0 (permutation test FDR-corrected p<0.05, 1000 permutations). **k.** LFP in depth across events around micro-arousal (top) and REM (bottom) states onset (red lines indicate state onset and offset).

Sleep spindles are coupled to global infra-slow and local slow LFP dynamics

The correlation between infra-slow LPF and micro-arousals suggests that fluctuations in the LFP during SWS could be linked to changes in neuronal synchrony expressed in the amplitude of sleep spindles. This result, together with the topographically matching oscillatory and infra-slow sources during HVS calls for a direct investigation of the topographical coupling between infra-slow and slow LFP dynamics and sleep spindles during SWS beyond overt micro-arousals. To address this question, we first characterised the local generators of sleep spindles and then evaluated their coupling to infra-slow and SO dynamics.

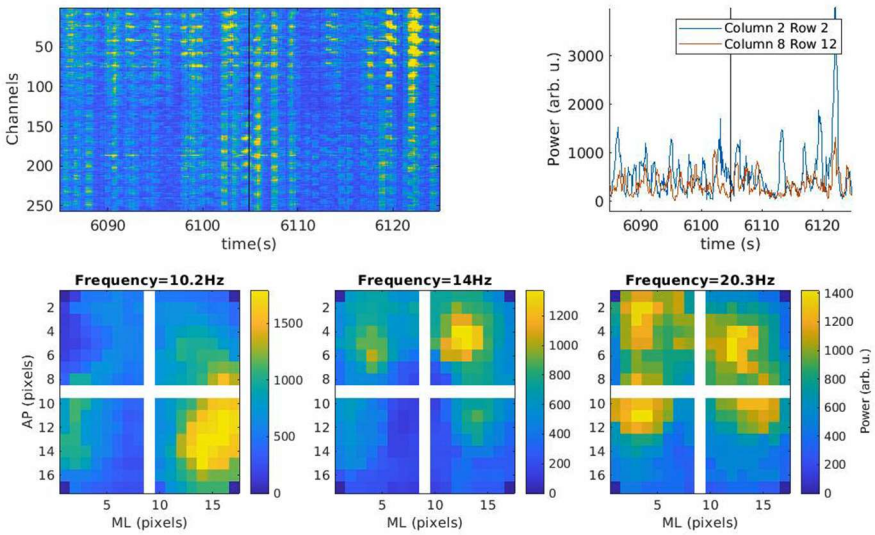

Movie 3| Spindle power (log-transformed and z-scored) across channels (top-left) and the traces from two channels (top-right). The three displays below show the spectral content at three different frequencies across frames (a spatial median filter with a 3x3 kernel was applied).

Inspection of the sigma band (10-20Hz) power dynamics reveals topographically structured patterns that presumably reflect the activation of various cortico-thalamic networks involved in the generation of sleep spindles (see Movie 3). To characterise the diverse spatio-spectral dynamics in the sigma band, we decomposed the power spectrograms across channels and frequency bins using factor analysis[47] (see Methods, Fig. 5a,b and Supplementary Information S12). The spatio-spectral structure of the factor loadings reflected diverse oscillatory modes (Fig. 5c) with their respective factor score dynamics displaying transient bouts corresponding to waxing and waning oscillations in the anatomical location and at the frequency reflected by the factor loadings (Fig. 5d). The dynamics of these factors represent a lower-dimensional description of the spatio-temporal variation of sigma power as illustrated in Fig. 5e. Group statistics revealed comparable factors across animals (Fig. 5f and Supplementary Information S10) with stereotypical burst durations (0.73±0.25s across animals and

factors, Fig. 5g) and harmonic index, a measure of spectral concentration (0.78±0.80, across factors and animals, Fig. 5h and Methods). Spindles in anterior areas (mostly somatosensory cortex, Fig. 5f) present larger amplitude compared to spindles in posterior areas (mostly posterior-parietal and retrosplenial and visual cortex, Fig. 5f) (Fig. 5i, paired t-test between the median spindle amplitude across bins in the AP axis).

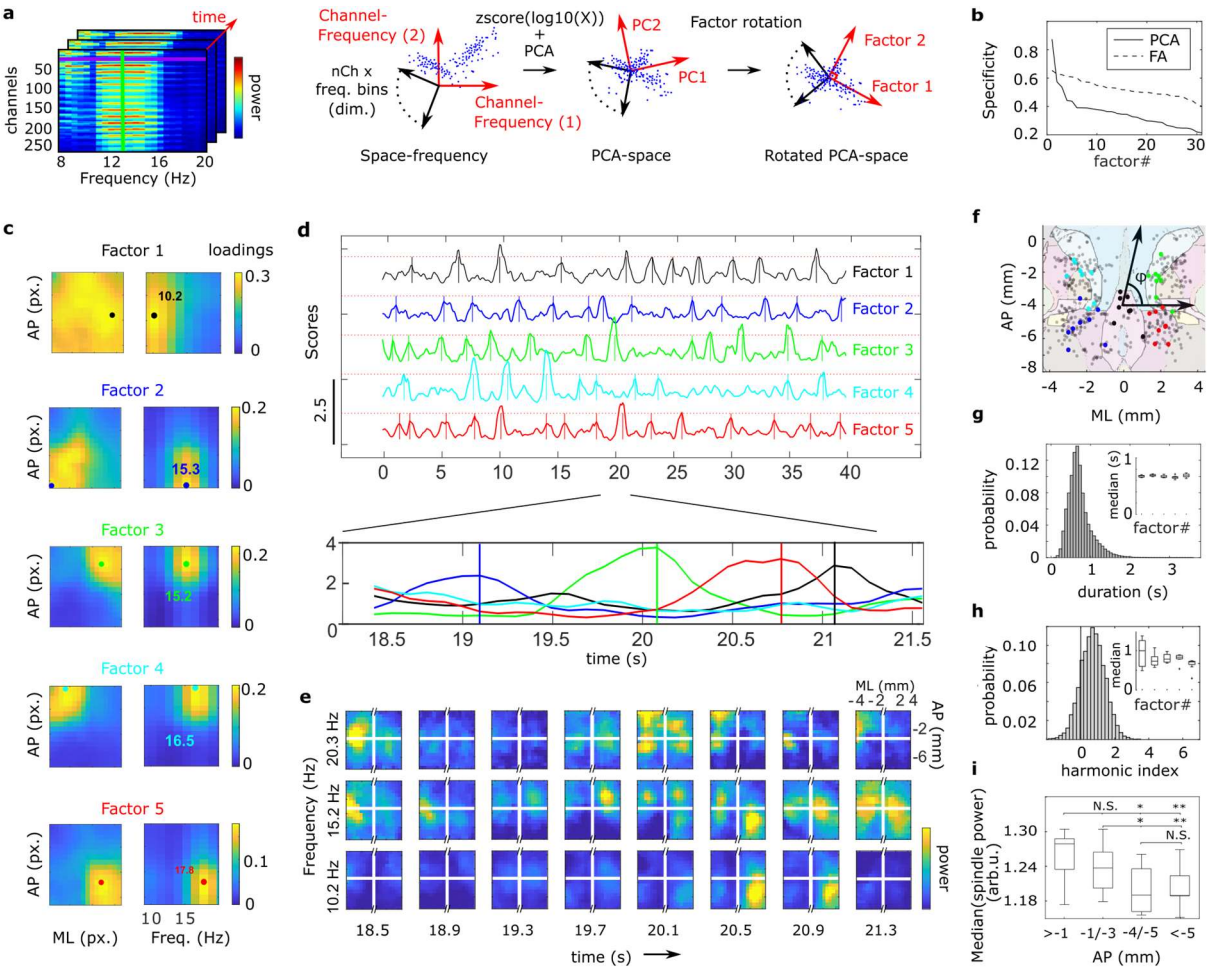

Figure 5| Detection of diverse local sleep spindle generators from the cortical surface. a. Schematic representation of spatio-spectral factor analysis. From a high-dimensional spatio-spectral space (left), factor analysis finds the most parsimonious modes of spatio-spectral covariation (right). **b.** 95 percentile of the specificity distribution across factors for PCA and rotated factors (FA) sorted by specificity. **c.** Spatio-spectral loadings of the first five factors for an example animal. Filled circles mark the position in space and frequency of the maximum loading. **d.** Score dynamics for the first five factors in panel c. The bottom plot shows overlapping traces in a zoomed-in window. **e.** Example of power dynamics at three different frequencies (rows) across frames (columns) corresponding to time points shown in d. **f.** Position of loadings peak in space (first 30 factors per animal). Coloured dots correspond to matching factors (n= 8 animals). The colour code is the same as in panels c and d. The atlas in the background is the same as in Fig. 2f. **g.** FWHM duration distribution of score peaks across the first five example factors. The inset describes the median of sleep spindle duration (in seconds) for all matched factors across animals (n=8 animals). **h.** Harmonic index distribution across factors for an example animal. The inset shows the median of the harmonic index for each of the matched factors across animals (n=8 animals). **i.** Median spindle power for all factors localized across the AP axis (n = 8 animals). Paired t-test, * p-val<0.05, ** p-val<0.005.

Having characterised the transient oscillatory modes of sleep spindles, we sought to identify the sources that underlie the temporal dynamics of their occurrence. As prior work has identified that infra-slow cardio-vascular and neuromodulatory fluctuations modulate sigma power and microarousal

states were associated with topographic and depthwise infra-slow fluctuations (Fig. 4c, d), we investigated whether these fluctuations in the LFP exhibit similar spatial profiles and modulate synchrony of SWS state and the occurrence of sleep spindles. Indeed, infra-slow LFP during SWS presented oscillations that were characterized by the same topographic pattern across the AL and PM regions (Fig. 6a and 6b) and the phase reversal around cortical L-IV (Fig. 6a and 6c) as those associated with synchronous HVS and SWS states. These spatial patterns of synchronous states thus were recapitulated in the microstructure of SWS synchrony reflected by the infra-slow LFP dynamics suggesting a common generating mechanism. We detected the troughs in the infra-slow LFP in the anterior-lateral region of interest (-4.2mm, -1.5mm / ML, AP), linked to larger DC-potential changes during SWS (Fig. 4g), and computed their cross-correlation with the occurrence of sleep spindles in different locations (anterior-left/right and posterior-left/right). Independent of their spatial localization, sleep spindles were consistently locked to the surface-negative phase of the infra-slow oscillation (Fig.6d and 6e). The fact that infra-slow fluctuations globally modulate local sleep spindles suggests that, although the detected spindle generators are orthogonal and present a low degree of overlap at a faster time scale (Fig. 5b,d), their rate is strongly correlated at the infra-slow time scale (Supplementary Information S14). In turn, the level of global synchrony of the SWS state, reflected by the spindle rate, is strongly coupled to infra-slow dynamics marked by the topographic and depth-reversing LFP patterns.

Thalamocortical sleep spindles are well-known to be modulated by the SO as they are induced by cortico-thalamic excitation provided by the Up states[57]. We therefore investigated whether the coupling between the SO dynamics in the LFP and sleep spindles could present topographical specificity. Inspection of the raw signal suggests the well-known coupling between global oscillations, with a phase reversal around L-IV, and sleep spindles. Moreover, a second-order topographical modulation became apparent from the raw data (Fig. 6f). To quantify this observation, we computed the phase distribution for global SO at the spindles time, which confirmed the occurrence of spindles at the peak of the global surface slow waves, i.e. Up state of the SO[58] (fig. 6g). Global slow negative waves detected on the surface were paralleled with a depth pattern that had a phase reversal around L-IV linked to SO Down states[59] (see Supplementary Information S15). Following the validation of the temporal coupling between SO and sleep spindles, we investigated the topographical relation between the amplitude of SO and the amplitude of sleep spindles. The trough-to-peak amplitude for the preceding trough and concurrent positive wave showed a stronger correlation at the location of spindles (Fig. 6h, i). This coupling was also significant for the preceding trough and the concurrent positive wave separately, but weaker for the trough following spindles (see Supplementary Information S16). These results reveal that the magnitude of local Down-Up state transitions biases both the timing and the amplitude of the local sleep spindle oscillations occurring during the Up state.

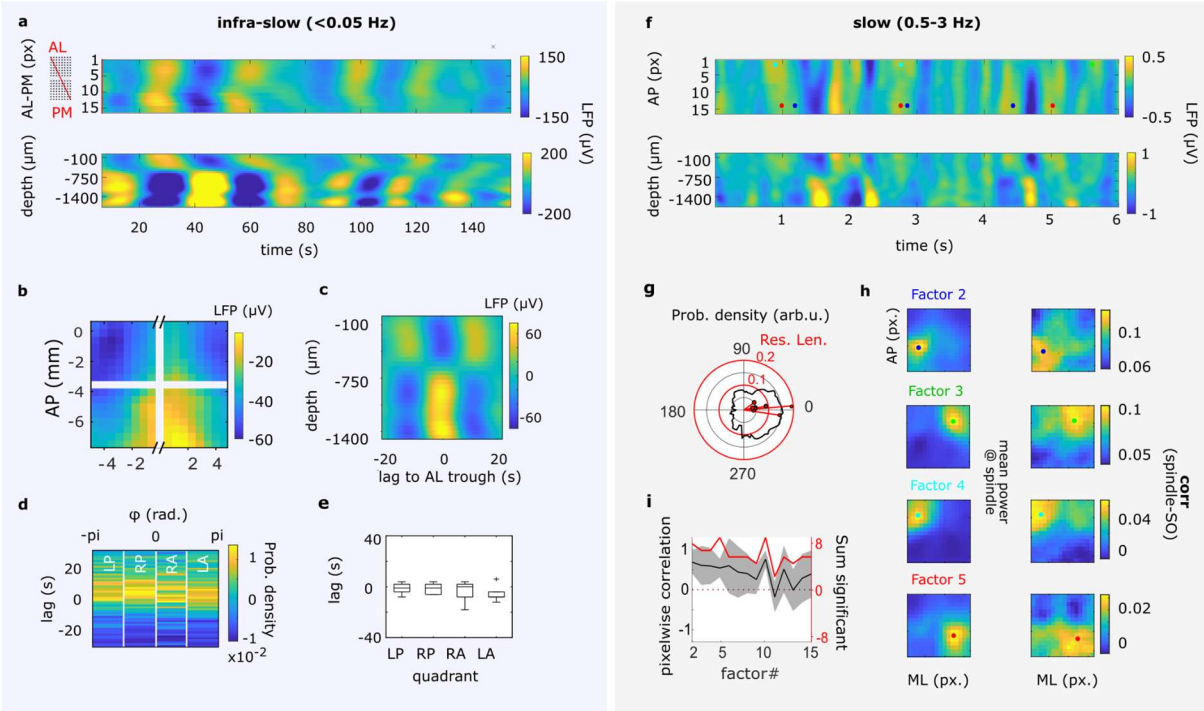

Figure 6| Coupling between infra-slow and slow LFP and local sleep spindles. a. Example of the infra-slow LFP in the AL to PM axis (top) and simultaneous recording across cortical layers (bottom). **b.** Mean infra-slow LFP (<0.05 Hz) triggered at the trough in AL channels. **c.** Mean infra-slow (<0.05 Hz) LFP profile across cortical layers. **d.** Cross-correlation between spindles and the troughs in the AL infra-slow (<0.05 Hz). **d.** The time lag of maximal cross-correlation across animals and ECoG quadrants (no significant differences observed between different quadrants, paired-sample t-test). **f.** LFP in the 0.5 - 3 Hz band for the 16 channels in the fourth column from the left of the array (top). The coloured dots correspond to the time stamps for the spindles detected with factors 1 to 5 represented in Fig 5c and 5d. The simultaneously recorded infra-slow LFP is shown below. **g.** In black, the distribution of the phase of SO at the time of a spindle accumulated across animals (n=8) and factors 1–10 sorted by variance. In red, the resultant vector for the phase of SO at the time of spindles for factor 1-10 is shown for all 8 animals separately. **h.** Left: mean spindle band power at the spindle time points for an example animal for factors 2 to 5 (same as in Fig. 5c and 5d). Right: the topographical representation of the correlation between the amplitude of the SO cycle and the Up-locked spindle amplitude for factors 2 to 5 (same as in Fig. 5c and 5d). **i.** The similarity between the power maps and the SO-spindle correlation maps is determined by computing the correlation between the maps in the two columns of panel h at the hemisphere of maximum loading. The mean and standard deviation of this topographical correlation across animals is shown for the first 15 factors sorted by variance. The right axis shows the sum of significantly correlated factors across animals for the first 15 factors (permutation test p<0.05, 1000 permutations).

Discussion

Multiplexed graphene micro-ECoGs to investigate large-scale oscillatory and infra-slow dynamics

Previous advances in flexible micro-ECoG arrays enabled increased sampling densities across large cortical areas[29–33]. However, the complexity of connectors and front-end electronics in non-multiplexed arrays constrained the scalability and miniaturization of recording systems[31,32]. On the other hand, systems based on high channel-count multiplexed flexible arrays have so far lacked the technological maturity for their application in chronic settings in freely moving animals[28]. Furthermore, detection of infra-slow activity with high channel-count recording systems has remained out of reach. Here, graphene-based active neural probes demonstrated reliable recordings of large-scale, high-density and wide-band epicortical and intra-cortical LFP in freely moving rats. The presented technology combines the advantages of wide-field imaging, in terms of DC-coupled

recording capabilities and spatial resolution, with the benefits of electrophysiological recordings, in terms of temporal resolution, broad-band sampling and allowing recordings during unconstrained behaviour. This combination of technical capabilities represents a unique window into the mesoscale synchronization within and between brain regions across a broad range of time scales and its relation to the underlying infra-slow spatio-temporal dynamics revealed by the infra-slow band of the extracellular potentials.

Leveraging these technical advancements we dissected the relation between large-scale spatio-spectral dynamics of the LFP, conventionally used to infer brain states and infra-slow dynamics, and spatio-temporal patterns of infra-slow (<0.5 Hz) field potential dynamics across brain states. Although the biophysical origin of infra-slow LFP is unclear[1], LFP at this time scale could emerge from slow changes in extracellular ionic concentration gradients generated by the synchronous activity of large neuronal populations constrained by metabolic and neuromodulatory factors[3]. The infra-slow LFP are likely reflecting the same dynamics that have been observed in numerous studies, including in derivatives of hemodynamics such as the blood-oxygenation-level-dependent (BOLD) signal[60,61], infra-slow fluctuations of ACh, NE and 5HT[4,5,55], fluctuations of power of oscillatory dynamics[6,14] and spiking of single neurons[9]. The evidence presented here, linking neuronal synchronisation reflected in mesoscale broadband LFP and topographically-resolved infra-slow LFP provides new insights into the origin of the infra-slow LFP and hints at the interaction between slow metabolic and neuromodulatory dynamics and neuronal synchronisation.

Brain-wide spatio-spectral brain state segmentation and characterization

Brain state dynamics are controlled by neuromodulatory systems that modulate the dynamics regimes of large-scale networks. Associated state-specific oscillatory dynamics synchronize neuronal populations across different spatio-temporal scales in both superficial cortical and subcortical regions giving rise to multiple spectrally distinct and spatially distributed sources that are reflected via volume-conduction in the LFP across the brain. Detecting these complex network states requires large-scale, dense, recordings capable of identifying cross-scale dynamics and localizing volume-conducted sources[34,45]. Combining high-dimensional spatio-spectral data with dimensionality reduction techniques offers the potential to discover subtle distinctions between brain sub-states[46] contributing to the improvement in brain states segregation. The detailed characterization of spatio-spectral features of brain states opens new avenues for therapeutical interventions. Previous studies have shown that electrical stimulation can influence brain regions across both local and long-range connections[62–64], creating large-scale network effects observable in the LFP[62]. Our findings support the design of closed-loop electrical stimulation therapies where the characterization of large-scale brain dynamics is critical. Identification of field potential sources in the infra-slow frequency band opens the door to the discovery of novel biomarkers of pathological states. Furthermore, detection based on infra-slow features could be advantageous for chronic neural implants where a reduction of the sampling rate implies a reduction in power consumption, with potential implications for seizure localization and prediction[65]. As the power and large-scale synchrony of the HVS increase with age[51] and rats used in the current study were young (ca. 4 m), we anticipate that the infra-slow dynamics we showed here provide a sensitive readout and could prove to be a complementary measure to detect and study the origin of this thalamocortical epileptiform activity. Topographic and laminar patterns of synchrony-associated infra-slow transients provide a guideline for their optimal detection in animals and urge for a translation of our results to the clinic for further use in human patients. Multi-channel recording systems, combined with stimulation electrode grids and control theory

strategies[63], could enable precise control of the dynamical state of large-scale networks, potentially down to transient oscillatory states such as HVS or sleep spindle oscillatory bursts.

Topographic characterization of sleep spindles and their coupling with SO

The segregation of brain states based on spatio-spectral features and their relation to infra-slow LFP can be extended to finer spatio-temporal scales by taking advantage of the dense, large-scale sampling of DC-coupled LFP recordings. Sleep spindles are thalamocortical oscillatory states which are linked to hippocampo-cortical communication[66,67] and consolidation of hippocampal-dependent and independent memories[66,68]. These oscillatory modes have been observed in various cortical regions with varying frequency modes both in humans and rodents[69–73], potentially presenting distinct roles depending on the engaged thalamocortical network. Our results represent an unbiased characterization of spatial and frequency localized sleep spindle oscillations that are consistent with and extend prior work. We were able to identify, detect and characterize localization, spatial extent and dominant frequency of diverse classes of spindle oscillations ranging from low frequency (~10Hz) global oscillations, as well as localized in anterior-posterior and lateral dimensions, higher frequency modes spanning a wide range of sigma frequencies and reaching lower beta range. Further analysis linking surface LFP topography of spindles with their intracortical sources and thalamocortical generators will provide further insight into the mechanisms underlying the diverse spindle oscillations.

The precise detection of local sleep spindles across cortical regions in freely moving animals and their time locking to slow and infra-slow dynamics could provide further insights into the mechanism by which these synchronous states facilitate memory consolidation in distinct cortical areas. SO have been shown to be local, i.e. engaging more strongly in certain cortical regions[2,58,68,74–76], and to play a key role in memory consolidation by coordinating cortico-hippocampal communication[66]. In turn, their entrainment of the sleep spindles following learning of various task modalities might reflect joint UP state and sleep spindle processing with distinct topographic role[58,68]. In this work, we show for the first time bilateral, large-scale and high-density mapping of slow waves and sleep spindles and evaluation of their local interaction. Our results reveal that while global SO dynamics entrains sleep spindles in a non-specific manner, the amplitude of the local slow oscillations correlates with the amplitude of local sleep spindles. This is consistent with local Down-Up state recruitment of localized spindles giving rise to a local K-complex. This observation highlights the physiological importance of the coupling between these two prominent cortico-thalamic rhythms and lays the foundations for the study of the functional role of local SO-spindle synchronization.

Qualitative model of the relation between neuronal synchrony and DC-potential shifts

The biophysical source of infra-slow field potentials remains unclear, with some works suggesting a non-neuronal origin[1]. Our characterization of synchronous oscillatory network dynamics and infra-slow LFP across cortical regions and layers provides new insights into the origin of infra-slow changes in the extracellular potential.

Using the brain states detected based on spatio-spectral features, we studied the infra-slow correlates of the hypersynchronous high-voltage spindle state and fluctuations within and at the transition out of SWS. Our results revealed a common source for the spike-and-wave discharge component of HVS and its DC envelope centred on somatosensory areas (Fig. 7a, left and Fig. 3i). Similarly, the topography of infra-slow fluctuations during SWS and around micro-arousals presented a gradient from somatosensory to medial and posterior areas (Fig. 7a, right and Fig. 4, 5). This gradient

matches the topography of sleep spindle power (Fig. 7a and Fig. 2g, 3i, 5i). The topographical alignment between the power of HVS and sleep spindles and their infra-slow correlates were complemented by the similarity of the depth profiles of the DC-coupled LFP. During HVS, the translaminar profile presented a phase reversal of the infra-slow potential around layer IV as well as for spike-and-wave discharges (Fig. 7b, left and Fig. 3). Similarly, infra-slow fluctuations during SWS and around the SWS/micro-arousal transitions showed a similar phase reversal around layer IV, which is comparable to the phase reversal of delta waves (Fig. 7b, right).

To explain these convergent observations, we propose a qualitative physiological model that unifies them and links neuronal synchrony to changes in DC-potential across states. During the synchronous phase of the HVS (the spike phase) and slow oscillations (Up-state) synchronous neural firing results in an increase of intracellular Ca^{2+} concentration. This leads to activation of the outward multiple K currents, most prominently, calcium-dependent potassium current (I_{K-Ca})[77] that are responsible for termination of the active state, repolarization of the membrane potential and an increase in extracellular potassium concentration ($[K^+]_o$), (Fig. 7b). These hyperpolarizing currents are larger in layer V where there is higher recurrent excitation[78] and, likely, higher net current density of I_{K-Ca} leading to a peak in the second derivative of the K^+ efflux and to a localized current source in this layer during the delta wave[67] or HVS wave[79] (Fig. 7c). During the wave phase of HVS or the down-state, the extracellular potassium ions are buffered by glia[42] and pumped in the cell by Na-K pumps. However, under repeated activation of K conductance during synchronous activity these mechanisms are not sufficient to return the $[K^+]_o$ to the baseline, resulting to a build-up of $[K^+]_o$ leading to a state-dependent $\Delta[K^+]_o$ (Fig. 7d, e)[41,42], which can have a sustained layer 5-dominance[41] matching the delta/HVS wave profile (Fig 5e). Here, we propose that these sustained $[K^+]_o$ gradients during states of high synchrony will lead to the generation of sustained dipoles by activation of the electrogenic NaK-ATPase pump, which pumps 2-K^+ in and 3-Na^+ out of the cell at a concentration-dependent rate[80] (Fig. 7f, h). In this manner, the sustained and layer 5 localized concentration gradient of $[K^+]_o$ would be a consequence of neuronal synchrony, giveing rise to depth-reversing DC dipole (Fig. 7h) and at the same time could causally influence the network dynamics by increasing the resting potential of neurons. This causality could be reflected in the relation between larger SO (larger increase in $[K^+]_o$) and higher excitability during the following Up-state as reflected in the amplitude sleep spindles (Fig. 7g).

Relation between infra-slow potentials, the sleep microstructure and neuromodulatory activity

Previous studies have shown the relation between neuromodulatory dynamics during SWS and in the SWS-REM transition[4,5,52–55] and sleep spindles occurrence, which co-fluctuate at the infra-slow time scale of 0.01-0.05Hz, often referred to as ultra-slow[81]. However, the mapping of infra-slow potentials across sleep sub-states remained limited to full-band EEG (fb-EEG) studies[56]. The interpretation of DC-coupled recordings poses a challenge in the interpretation of the signal polarity[82], given the lack of a stable absolute potential reference. Based on our model of DC-potential shifts generation by sustained translaminar $[K^+]_o$, we argue that referencing the DC-potential to the desynchronized states (i.e. micro-arousals and REM) in contrast to SWS results in accurate characterization of the topographical changes.

Our results demonstrate the correlation between sleep sub-state dynamics and infra-slow LFP, which are topographically structured and parallel neuromodulatory dynamics. The observed infra-slow LFP dynamics also uncover states of increased arousal level reflected in extremely subtle (<0.5mm/s) movements during SWS. This is consistent with the relation of neuromodulatory dynamics

to overt and covert micro-arousals[4]. Future studies should address the relation between neuromodulatory activity and infra-slow LFP directly by combining DC-coupled electrophysiological recordings and photometric or amperometric recordings of neuromodulatory dynamics. Following the discovery of local modulation of up-down state transitions by cholinergic activity during REM sleep[16], future studies could investigate the local correlations between infra-slow LFP and delta waves as well as local neuromodulatory activity. The potential relation between infra-slow LFP and $[K^+]_o$ gradients is particularly promising in light of recent findings on the role of local $[K^+]_o$ in affecting neuromodulatory regulation of sleep and behavior[83].

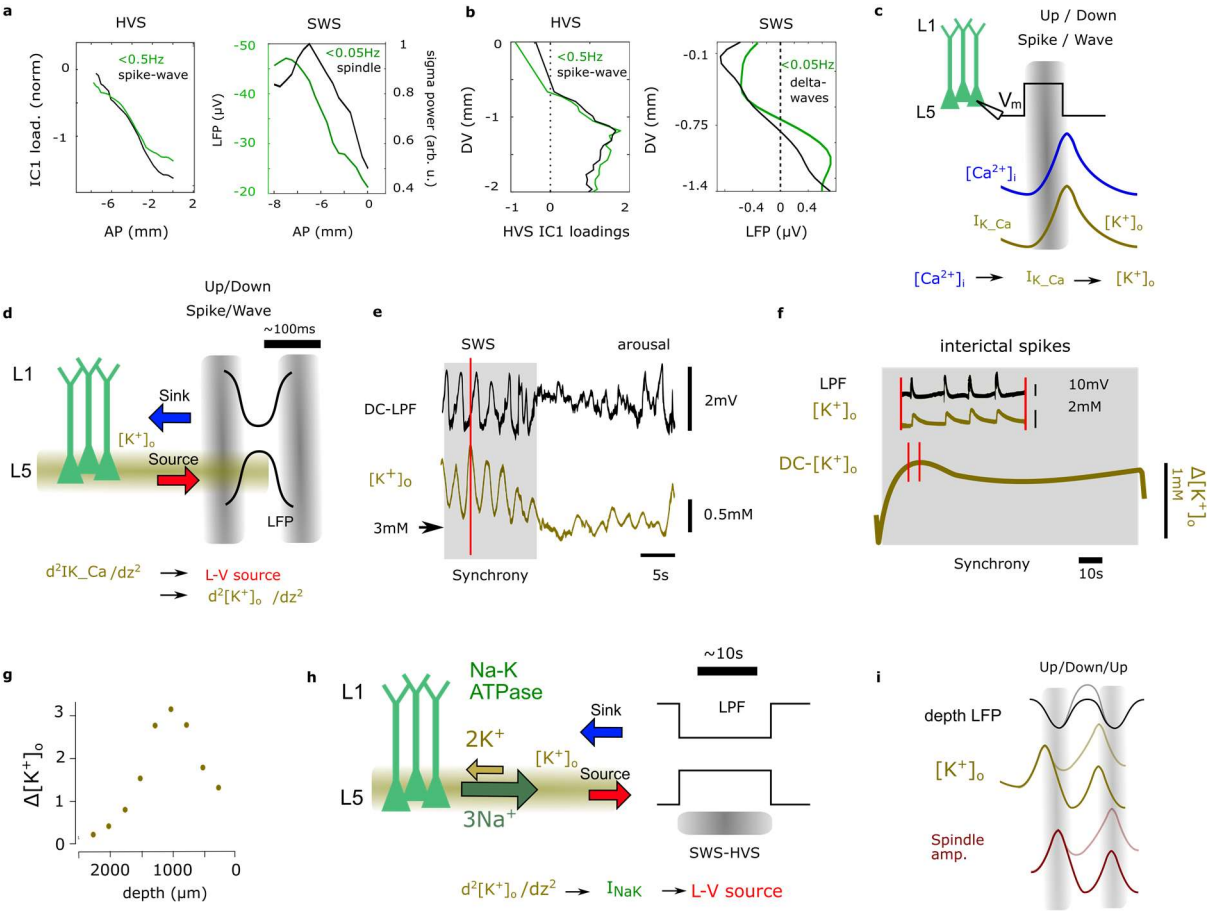

Figure 7| Qualitative model of the link between synchronous states and DC-potential changes. a. Topographical relation between the amplitude of spike-and-wave discharges and their infra-slow correlates (left) and between the power of sleep spindles during SWS and mean infra-slow LFP at the AL troughs (right). **b.** Translaminar profile of the HVS spike-and-wave amplitude (left) and its infra-slow correlates (right). **c.** Synchronous states such as up states and the spike component of HVS drive an increase in intracellular calcium, which leads to the opening of K^+ channels that hyperpolarize the neurons. **d.** The increase in K^+ conductance during the up-down state transition is larger in layers with high neuronal activity, leading to an LFP source around L-V and generation of a K^+ gradient around this layer. **e.** Empirical evidence for the relation between extracellular potassium concentration and slow oscillations as well as its DC level change between SWS and desynchronized states (adapted with permission from Seigneur et. al. 2006[42]). **f.** Experimental data showing the buildup of $[K^+]_o$ during an induced trace of interictal spikes (adapted with permission from Moody et. al. 1976[41]). **g.** Depth profile of the amplitude of this buildup (adapted with permission from Moody et. al. 1976[41]). **e.** The buildup of a change in the layer-specific DC-level of potassium leads to a layer-specific activation of the electrogenic NaK pump, which in turn generates a DC LFP source. **f. g.** Schematic of the relation between the amplitude of slow oscillations, potentially generated by changes in the potassium conductance during the down state and the accumulation of potassium in subsequent cycles leading to increased excitability and sleep spindle amplitude.

Relation between infra-slow potentials, potassium and vasomotor dynamics

Increased $[K^+]_o$ can trigger vasomotor activity by the inward-rectifying channels in blood vessels, coupling the neuronal activity to the blood flow and oxygenation level[1]. Previous works showed that blood vessels present a different potential than the extracellular space, leading to extracellular infra-slow potential variations caused by vasomotor dynamics[1], leading to the notion that this might be the only biophysical mechanism behind infra-slow LFP generation. Here, we provide two arguments against this mechanism as the main source of the infra-slow LFP. Firstly, micro-arousals and REM present opposite vasomotor dynamics at the transition from SWS[84,85], therefore, the observation of comparable spatiotemporal infra-slow dynamics around these two state transitions, supports our alternative model. Secondly, the translaminar phase reversal in the LFP that we observed cannot be explained by potentials induced by vasomotor dynamics. Rather than vasomotor dynamics dominating the generation of extracellular infra-slow potentials, our model supports that the laminar-specific changes in $[K^+]_o$ that generate sustained dipoles could also contribute to the delayed vasomotor dynamics. This could be the mechanism linking topographic infra-slow potentials measured by fb-EEG and resting state networks from the BOLD signal[27].

Conclusion

Large-scale, DC-coupled LFP recordings enabled by multiplexed graphene neural probes provided insights into the topographical and translaminar relation between neuronal synchrony and infra-slow LFP dynamics. These results expand our understanding of cross-frequency coupling across brain regions and states, providing new insights into the mechanisms of cortical excitability and sleep regulation with implications in clinical and fundamental neuroscience.

Methods

Graphene probes microfabrication

Large-scale graphene neural probes were fabricated on a 4” wafer following the procedure described before[39] with minor modifications. An initial 4µm-thick polyimide (PI-2611, HD MicroSystems) was spun-coated on a Si/SiO_2 4” wafer and baked at 350°C. Polyimide was chosen as a substrate due to its stability and biocompatibility[33,44,86,87]. A first metal layer 30nm Ti for adhesion, 300nm Au for conductance and 10nm Ni as diffusion barrier at high temperatures) was deposited by electron-beam vapour on a previously photodefined negative AZ 5412E (Clariant, Germany) and then structured by a lift-off process. Then, a 2µm-thick polyimide interlayer was deposited to separate metal layers and vertical interconnection access (VIA) holes opened using a 200nm-thick Al mask (by lift-off using AZ 5412E, and etching by O_2 plasma. Afterwards, the graphene grown by chemical vapour deposition on Cu was transferred (process done by Graphenea). Graphene was patterned by oxygen plasma (50 sccm, 300W for 1min) in a reactive ion etching (RIE). The photodefinable resist used to protect the graphene in the channel region was HIPR 6512. After the graphene etching, a second metal layer was patterned on the contacts following the same procedure as for the first layer, but this time performing an ozone cleaning treatment before metal deposition in order to improve the contact resistance and noise[88]. Subsequently, the transistors were insulated with a 3-µm-thick photodefinable SU-8 epoxy photoresist (SU-8 2005 Microchem), keeping uncovered the active area of the transistors channel. SU-8 is known to limit the stability of devices in physiological conditions to a semi-chronic time scale[89,90]. Finally, the polyimide substrate was structured in a reactive ion etching process using a thick AZ9260 positive photoresist (Clariant) layer as an etching mask. The neural probes were then

peeled off from the wafer and placed in a zero insertion force (ZIF) connector to be interfaced with our custom electronic instrumentation.

Ethical approval and animal handling.

The experiments in-vivo were in accordance with the European Union guidelines on the protection of vertebrates used for experimentation (Directive 2010/63/EU of the European Parliament and of the Council of 22 September 2010). Electrophysiological experiments with Long Evans rats were carried out under the German Law for Protection of Animals (TierSchG) and were approved by the local authorities (ROB-55.2-2532.Vet_02-22-22). Rats were kept under standard conditions (room temperature 22 ± 2 °C, 12:12 h light–dark cycle, lights on at 10:00), with food and water available ad libitum.

Surgical implantation of large-scale graphene ECoGs

A cohort of 8 Long Evans rats, weighing between 558±121 g were used for this study. As previously described[37], anaesthesia was induced with Midazolam (2mg/kg), Medetomidin (0.15mg/kg) and Fentanyl (0.005mg/kg). After 1h of surgery, isoflurane at a concentration of 0.5-1.5% was provided while monitoring vital signs. The posterior-dorsal area of the head was shaved, the skin was locally disinfected with Povidone-iodine and subcutaneously infiltrated with the local anaesthetic Bupivacaine. The skin was then incised and the dorsal skull was cleaned carefully by blunt dissection and the temporal muscle was separated from the skull. The skull was cleaned with H_2O_2 (3%) and phosphoric acid (KERR - Gel Etchant, 37% phosphoric acid), sequentially for a few seconds and then by scratching the surface with a scalpel. A 3D printed base ring made of Polylactic acid (tough PLA, Ultimaker) was anchored to the skull with at least six screws in the frontal side of the skull, two more on each temporal plate of the skull, two on the occipital plate and with Metabond cement (Parkell).

After at least 7 days of recovery, the animals underwent a second surgery following the same anaesthetization procedure described above. For these longer surgeries (~8h), Metamizol (110mg/kg) was provided in order to maintain the analgesic effect 4h after the start of the surgery. A small craniotomy (~3mm in diameter) was opened above the cerebellum for the placement of an Ag/AgCl reference electrode (100µm thick) close to the cerebellar surface. In order to minimize the contact of Ag with the tissue and improv the electrochemical stability of the reference, the electrodes and the cerebellar surface were covered with a drop of agar solution (0.5%). Secondly, a large craniotomy was opened on the frame defined by the base-ring with a width of 1.1cm and length of 1.3cm. In order to perform such a large craniotomy, the skull was removed in five pieces. Four symmetric quadrants and the skull on the midline. For the detachment of the skull from the dura, a blunt tool was used, with special care on the area around the sinus. Afterwards, the dura was removed within the area of the craniotomy and the device was placed in its final position (see Supplementary Information S3). The craniotomies were covered with prepolymerised PDMS (~100µm thick – same composition as above) and sealed with Vetbond (Animal Care Products, USA). A 3D-printed skull replacement was then lowered using the stereotaxic Microdrive until the PDMS surface and slightly compressed by ~200µm to correct the brain bulging and fixed in place with optical cement. The cranial window was filled with dura-gel (Cambridge Neurotech) in order to seal the cable of the probe.

Implantation of flexible depth probes.

For the insertion of flexible depth probes, rigid silicon shuttles with polyethylene glycol (PEG) 10000MW were used as previously reported[44,91]. Flexible depth probes were aligned with the silicon shuttles with previously added PEG using a micromanipulator under the microscope. When properly

aligned, the PEG was molten on a hot plate. In order to have finer control of the placement of the connectors during implantation, the shuttle was attached to an additional motorised stage on the stereotaxic frame. After insertion of the depth probe into its final location, the PEG was dissolved using physiological saline solution. Once the flexible probe was delaminated from the shuttle, it was immobilised using a thin layer of agar (0.5% mass) after cooling down (shortly before solidifying). Subsequently, the additional motorised stage was used to extract the shuttle without moving the flexible probe or its connector. Finally, the probe was fully immobilised using optical cement (Evoflow - Ivoclar Vivadent, Liechtenstein) and the connector moved to its final position using the stereotaxic frame.

Electrophysiological recordings

Electrophysiological recordings using the large-scale graphene probes and depth graphene probes were carried out in a circular open field arena (0.8m in diameter) with high walls transparent to IR light for motion capture tracking. The recordings lasted between 46 minutes and 248 minutes (mean of 145.8 minutes). The discrete electronics system was based on a previous version[40], upscaled to enable the operation of up to 256 channels. Shortly, the system consists of a commercial data acquisition card (National Instruments DAQ-Card, USB-6363), and a custom-built amplification front-end and switching array for multiplexing (see Supplementary Information S1). The sampling frequency of the DAQ-Card of 1MHz is shared among the 256 channels, the DC-coupled and AC-coupled amplification stages. For each switch between columns 2 samples are dropped for signal stabilization leading to a sampling frequency of 651Hz each channel. This system was operated using the code published in the repository (https://github.com/RamonCortadella/LargeScale-WideBand/) for the acquisition of calibration $I_{ds} - V_{gs}$ curves as well as for brain mapping. In the second system, an ASIC[38] implements the switching matrix, I-V conversion with offset cancellation and further amplification and digitization with a correlated double sampling. An FPGA on the headstage implements the digital communication between the ASIC and an interface board (IFB, Multi-Channel Systems and MCS-SCU-in-vitro, Multi Channel Systems) to implement the data transmission to the headstage. The system was operated using customised software from Multi-Channel Systems. The sampling frequency was 12 kHz per channel, way above the LFP band, to reduce high-frequency noise (see Supplementary Information S2).

Signal pre-processing

The acquired signals representing the drain-source currents through all transistors in the active matrix were calibrated using the stationary transfer curve ($I_{ds} - V_{gs}$) by interpolating the DC-coupled current. Using this method, variations in the G_m due to V_{gs} drifts are corrected[92]. Following interpolation, the signals were high-pass filtered using a median filter with a time constant of 200s, which preserves better changes in the abrupt changes in the DC-potential level compared to IIR filters. The signals were converted to a binary format (16-bit) with a range of 10mV for full-band recordings (ASIC-based system), 30mV for DC-coupled channels (discrete-components-based system) and 3mV for the AC-coupled channels (discrete-components-based system). Bad channels were then detected as outliers (x330 or /330 times the power) in the low frequency (1-10Hz) or high frequency (60-120Hz) within neighbouring 3x3 pixels. The bad channels were then interpolated using the "scatterinterpolant" function in Matlab, and was median-filtered with a 3x3 kernel and using constant padding.

Data analysis

Spectrogram calculation

Spectrograms were computed using the multitaper method on the whitened signal. Whitening was performed using a first order autoregressive model fitted on the LFP in the 1-100Hz band (excluding the 50Hz and 100Hz pick-up noise peaks by a notch filter). The window length for the FFT was 2.36s (or 2.46s for the 512 channel probes). The overlap between FFT windows was half of the FFT window duration. The spectrograms for factor analysis of sleep spindle power were computed with a window of 197ms (and an overlap between FFT windows of half the window duration).

Brain states classification

Brain state classification was based on the combination of behavioural states obtained from motion tracking and electrophysiological states obtained from the high channel-count neural probes (see Results section). Motor state classification was based on thresholding the speed modulus (with a speed of 5mm/s) to define periods of activity and inactivity (>5s) and motor-defined "sleep" starting after 20s of inactivity and lasting at least 20s more). The electrophysiological states (i.e. SW, theta and HVS) classified from spectral characteristics were median filtered in order to eliminate exceedingly fast transitions. SW and theta states were filtered with a time constant of 20 s and HVS states with a time constant of 1.5s. Then, the electrophysiological states were combined with the motor state for complete brain state classification. SWS was defined as overlapping periods of sleep and SW activity. Awake non-theta (Aw. non-theta) states were non-sleep periods overlapping with SW state. THE (exploratory state) is comprised of overlapping theta and active state. For REM classification, the active/inactive state was median filtered with a time constant of 20s to exclude brief movements during REM. Electrophysiological states classified as theta that were overlapping with presumed sleep states were classified as REM when preceded by SWS. HVS events were defined solely based on the electrophysiological classification. Finally, micro-arousals were defined as bouts of active state shorter than 10s within 40s of inactivity and limited to SWS (with these short bouts of movement not interrupting the SWS epochs).

Measurement of separation between state clusters

Quantification of the separability of brain states was evaluated using rescaled Mahalanobis distances. More precisely, the Mahalanobis distances for all data points with respect to the points in a particular state were computed. Then, the Mahalanobis distances of all points that do not belong to that particular state were rescaled and summed. The rescaling was according to the complementary of the cumulative chi-squared distribution with 2 degrees of freedom (number of dimensions in our UMAP embedding). Using this rescaling, those points that are nearer to the cluster of the particular state, but do not belong to it have a higher contribution. The summed distance divided by N is the *L-ratio* used to quantity the separability of states[93]. The larger the *L-ratio*, the less isolated is the given cluster.

Computation of mean spectrum across cortical regions and states

The mean spectrum was computed from the spectrogram across samples for each brain state. The mean spectrum was re-whitened in each state separately by performing a linear detrend on the log-transformed mean spectrum. The linear fit from a single channel (second row and second column) was used for all channels. The log-transformation on the rewhitened spectrum was reversed and the mean power within various bands was computed as displayed in Fig. 2g. Arbitrary units are used as the whitening distorts the original scale. To compare the mean power across states, frequency bands

and animals, the mean power in the AP axis was computed, its mean subtracted and normalised by its range (maximum minus minimum).

Independent component analysis of wide-band LFP around HVS

LFP was band-pass filtered in the 5-30Hz band and separately low-pass filtered below 0.5Hz. Epochs around the onset of HVS (±20s) were detrended, their median subtracted and concatenated. Then, the "fastica" algorithm implementing ICA was run. The activation dynamics of all independent components (ICs) were used to compute the reconstructed LFP for each component by multiplying the maximum loading value and its activation score. The first peak in the signal following HVS onset was detected from the reconstructed LFP below 0.5Hz, or from the RMS of the reconstructed LFP (for ICs from the 5-30Hz band). The cross-correlation peak at positive lags between the peaks and the HVS onset was computed. Subsequently, the RMS power of the reconstructed LFP at the loadings peak was computed in both bands. The rank of ICs for these two metrics (cross–correlation and RMS power) was summed up and used to sort the ICs. The loadings of the first component were compared across animals after normalizing the loadings by their value at -3.5mm with respect to bregma (AP axis) and 3.5 with respect to the midline (ML axis). The product between the peak cross-correlation and RMS of the reconstructed LFP, normalized by its maximum value across ICs was used to define an IC-relevance index.

SVD of infra-slow LPF and analysis of temporal relation to state transitions

The preprocessed LFP during SWS and REM plus the preceding and following the20s was concatenated across sessions for each animal, filtered below 0.5Hz and rank transformed to reduce the impact of motion artefacts on the decomposition. The SVD of the transformed signal revealed the common second component across animals. To compute the interevent interval of troughs during SWS we took the rank-transformed signal during the entire sleep block, detected the troughs in the score of SV2 and kept those events in the 90th percentile of prominence within SWS only. We used these events to compute the cross-correlation of troughs with micro-arousals. The cross-correlation between troughs and REM sleep onsets was computed by taking the troughs in the 90th percentile in terms of prominence within the entire sleep block.

Triggered average of infra-slow LFP and spindle/low-gamma power around states onset

To compute the triggered average, the preprocessed LFP was low-pass filtered below 0.5Hz and the signal within the micro-arousals (0.7s post onset) or REM sleep epochs (10s post-onset) substracted in the time window of interest (±30s for micro-arousals and ±150s for REM sleep).

Correlation between states duration and LFP shifts duration

The baseline median and standard deviation were computed from the SV2 score in the 20s preceding the state onset across events. The duration of the trough was calculated as the time the SV2 score remains under the threshold (baseline minus half the standard deviation) after the state onset (within a period equal to the duration of the longest epoch). The Spearman correlation was limited to events shorter than 60s for REM which presented a significant correlation with SV2 score shifts. The correlation between the duration of negative LFP shifts in deep layers and the states duration was computed similarly, but in this case, all REM events were considered.

Identification of putative down-states for depth probe position estimation

The LFP signal during SWS from ECoG recordings was filtered in the delta band (0.5-3Hz) and the mean across pixels taken at any time point to have a measure of global delta waves. The large amplitude

troughs (>2 x standard deviations) were detected, which presented a phase reversal across layers in almost every instance (see Supplementary Information S14).

Factor analysis

Factor analysis was performed as previously described[47]. Briefly, it consists of the following steps. First, the power per frequency bin and channel is log-transformed to bring the distributions closer to symmetric (normal) and then zscored to have homogeneous variance across all dimensions. The spectrogram is also spatially filtered for each frequency bin and time point using a 3x3 median filter across pixels. Then principal component analysis is performed and 99.9% of the variance is kept. Factor orthogonal rotation was then performed using the Varimax method[94], using the simplicity criteria to obtain a matrix of factor loadings. The simplicity criterion finds directions with the most parsimonious structure in the covariance matrix, which have high loadings in only a few spatio-spectral variables and close to zero in most of them. In addition, factor loadings are all positive which eliminates the ambiguity in the polarity of principal components.

Specificity calculation

The spectrogram in the sigma band was spatially filtered (using a 3x3 median filter across pixels) for each frequency bin and time point. Then the spatial-frequency coordinates with a loading above half of the maximum were taken as the signal and those below as the noise. The ratio between the mean power of the signal and the mean power of noise was defined as the specificity of a factor to describe the covariance structure of the spectrogram in the sigma band.

Sleep spindle duration estimation

The duration of sleep spindles was computed from the activation dynamics of distinct factors. The activation reflects the projection of the log-transformed, zscored spectrogram on the direction of the loadings. This projection does not reflect a measure of reconstructed power but of log-transformed, zscored power. The log tranformation was reversed, effectively stretching positive deviations, and the duration was defined as the FWHM of the activation peaks. The traces shown in Fig. 5d correspond to the activations after reversing the log transformation.

Matching of factor loadings

For comparison of factor characteristics across animals, factor loadings from different animals are matched based on their Euclidian distance in a 7-dimensional feature space. The features used for matching are the sign in the ML axis, the sign in the AP axis with respect to the centre of the array, the actual position in the array in units of pixels (X and Y axis), maximum frequency in rescaled frequency axis (centred at 0 and normalised by the maximum variation of 5Hz). The number of channels with loadings above half of the maximum loading and the number of frequency bins with maximum loading above half of the maximum (both normalised by the number of channels in a quadrant of the grid) were also used.

Harmonic index calculation

The spectrogram was log-transformed and zscored to be in the same space used for factor rotation. Then its value was taken at all sleep spindle occurrence times (i.e. times of peaks in the activation of factors) at the location and frequency of peak factor loadings (and at ±5Hz). The power at the peak frequency minus the mean of the ±5Hz points defines our measure of harmonicity. The harmonic index can be interpreted as the number of standard deviations between the power at the frequency

of maximum loading and the power at 5Hz below and above (in the z-scored and log-scaled power space).

Temporal coupling between infra-slow networks activation and sleep spindles

The time difference between each of the spindle events from all factors and the troughs in the infra-slow LFP in an AL region of interest (-4.2mm, -1.5mm / ML, AP) were computed. Then, the JPDF for lags and the location of the spindle oscillator (defined as the quadrant with maximum loading using polar coordinates centered on the midline and at - 4mm from Bregma in the AP axis) was computed. The same distribution was computed from randomised time points within SWS periods for the gradient peaks and the JPDF recomputed from 10 randomizations. The mean JPDF from the randomised distributions was subtracted from the non-randomised JPDF in order to eliminate the edge bias produced by having gradient peaks close to the onset or offset of SWS epochs.

Coupling between slow oscillations and local sleep spindles

To evaluate the coupling between SO and sleep spindles we first evaluated the phase statistics of global SO at the time of peaks in scores of the first 10 factors for all animals by taking the phase of the mean LFP signal across the entire array. To show the preferred phase and strength of modulation for all animals separately we computed the resultant vector for the first 10 factors independently on each of the 8 animals. Once the temporal coupling was established, we looked into topographical coupling between SO and sleep spindles by calculating the correlation between the amplitude of the SO in all channels of the array and the amplitude of sleep spindles for each of the first 15 factors and each of the 8 animals. The amplitude of the slow oscillation was determined by finding the preceding trough (between 0.8 and 0.2s of the spindle time) and the peak (within 200ms of the spindle time) at the location of maximum loading. The SO amplitude at these times was computed for all channels and their correlation to the spindle score amplitude was calculated.

Statistical methods

Mean or medians are given with standard deviation. Significance testing of differences between distributions or deviations from zero was done by paired-sample t-test or by permutation test. The statistical significance of the positive and negative deviations from zero observed in the triggered average was assessed by a permutation test for each pixel and time point. The distribution of values for each combination was contrasted to the whole population (across pixels and time points). A subset of random points (same as the length of micro-arousal or REM events) was taken from the whole population and their median was computed. This process was repeated for 1000 permutations for each pixel-time pair and a p-value was extracted reflecting the fraction of randomizations that presented a median beyond the true median for that pixel-time pair. To take into account the false discovery for such a large number of comparisons we applied the Benjamin and Hochberg correction[95]. To evaluate the similarity between the correlation maps and the factor loadings, the correlation between these two maps in the hemisphere of maximum loading was evaluated. To check for the significance of the correlation, the pixels in the correlation map were shuffled and a p-value for the correlation was obtained (1000 permutations).

Data availability

The characterization of devices in-vitro and the complete electrophysiological and motor tracking dataset is available from the corresponding author upon request. Movies can be found in (https://doi.org/10.12751/g-node.ehj8yj).

Code availability

The complete code for analysis of electrophysiological data is available from the corresponding author upon request. Code for the operation of the custom-built recording system can be found in https://github.com/RamonCortadella/LargeScale-WideBand/

References

1. Drew, P. J., Mateo, C., Turner, K. L., Yu, X. & Kleinfeld, D. Ultra-slow Oscillations in fMRI and Resting-State Connectivity: Neuronal and Vascular Contributions and Technical Confounds. *Neuron* **107**, 782–804 (2020).
2. Alfonsa, H. *et al.* Intracellular chloride regulation mediates local sleep pressure in the cortex. *Nat. Neurosci.* **26**, 64–78 (2023).
3. Krishnan, G. P., González, O. C. & Bazhenov, M. Origin of slow spontaneous resting-state neuronal fluctuations in brain networks. *Proc. Natl. Acad. Sci.* **115**, 6858 (2018).
4. Kjaerby, C. *et al.* Memory-enhancing properties of sleep depend on the oscillatory amplitude of norepinephrine. *Nat. Neurosci.* **25**, 1059–1070 (2022).
5. Zhang, Y. *et al.* Interaction of acetylcholine and oxytocin neuromodulation in the hippocampus. *Neuron* **112**, 1862-1875.e5 (2024).
6. Watson, B. O. Cognitive and Physiologic Impacts of the Infraslow Oscillation. *Front. Syst. Neurosci.* **12**, (2018).
7. Palva, J. M. & Palva, S. Infra-slow fluctuations in electrophysiological recordings, blood-oxygenation-level-dependent signals, and psychophysical time series. *NeuroImage* **62**, 2201–2211 (2012).
8. Väyrynen, T. *et al.* Infra-slow fluctuations in cortical potentials and respiration drive fast cortical EEG rhythms in sleeping and waking states. *Clin. Neurophysiol.* **156**, 207–219 (2023).
9. Okun, M., Steinmetz, N. A., Lak, A., Dervinis, M. & Harris, K. D. Distinct Structure of Cortical Population Activity on Fast and Infraslow Timescales. *Cereb. Cortex* **29**, 2196–2210 (2019).

10. Raut, R. V. *et al.* Arousal as a universal embedding for spatiotemporal brain dynamics. 2023.11.06.565918 Preprint at https://doi.org/10.1101/2023.11.06.565918 (2023).
11. He, B. J., Snyder, A. Z., Zempel, J. M., Smyth, M. D. & Raichle, M. E. Electrophysiological correlates of the brain's intrinsic large-scale functional architecture. *Proc. Natl. Acad. Sci.* **105**, 16039–16044 (2008).
12. Liu, X., Leopold, D. A. & Yang, Y. Single-neuron firing cascades underlie global spontaneous brain events. *Proc. Natl. Acad. Sci.* **118**, e2105395118 (2021).
13. Vanhatalo, S. *et al.* Infraslow oscillations modulate excitability and interictal epileptic activity in the human cortex during sleep. *Proc. Natl. Acad. Sci.* **101**, 5053–5057 (2004).
14. Leopold, D. A., Murayama, Y. & Logothetis, N. K. Very Slow Activity Fluctuations in Monkey Visual Cortex: Implications for Functional Brain Imaging. *Cereb. Cortex* **13**, 422–433 (2003).
15. Collins, L., Francis, J., Emanuel, B. & McCormick, D. A. Cholinergic and noradrenergic axonal activity contains a behavioral-state signal that is coordinated across the dorsal cortex. *eLife* **12**, e81826 (2023).
16. Nazari, M. *et al.* Regional variation in cholinergic terminal activity determines the non-uniform occurrence of cortical slow waves during REM sleep in mice. *Cell Rep.* **42**, 112450 (2023).
17. Raut, R. V. *et al.* Global waves synchronize the brain's functional systems with fluctuating arousal. *Sci. Adv.* **7**, eabf2709 (2021).
18. Mitra, A. *et al.* Spontaneous Infra-slow Brain Activity Has Unique Spatiotemporal Dynamics and Laminar Structure. *Neuron* **98**, 297-305.e6 (2018).
19. Chan, A. W., Mohajerani, M. H., LeDue, J. M., Wang, Y. T. & Murphy, T. H. Mesoscale infraslow spontaneous membrane potential fluctuations recapitulate high-frequency activity cortical motifs. *Nat. Commun.* **6**, 7738 (2015).
20. Ma, Y. *et al.* Resting-state hemodynamics are spatiotemporally coupled to synchronized and symmetric neural activity in excitatory neurons. *Proc. Natl. Acad. Sci. U. S. A.* **113**, E8463–E8471 (2016).

21. Vanhatalo, S., Voipio, J. & Kaila, K. Full-band EEG (FbEEG): an emerging standard in electroencephalography. *Clin. Neurophysiol. Off. J. Int. Fed. Clin. Neurophysiol.* **116**, 1–8 (2005).
22. Binder, N. F. *et al.* Vascular Response to Spreading Depolarization Predicts Stroke Outcome. *Stroke* **53**, 1386–1395 (2022).
23. Aladjalova, N. A. Infra-Slow Rhythmic Oscillations of The Steady Potential of the Cerebral Cortex. *Nature* **179**, 957–959 (1957).
24. Higgins, C. *et al.* Replay bursts in humans coincide with activation of the default mode and parietal alpha networks. *Neuron* **109**, 882-893.e7 (2021).
25. Pedrosa, R. *et al.* Hippocampal ripples coincide with "up-state" and cortical spindles in Retrosplenial Cortex. 2022.12.19.521088 Preprint at https://doi.org/10.1101/2022.12.19.521088 (2022).
26. Osorio-Forero, A. *et al.* Noradrenergic circuit control of non-REM sleep substates. *Curr. Biol.* **31**, 5009-5023.e7 (2021).
27. Hiltunen, T. *et al.* Infra-slow EEG fluctuations are correlated with resting-state network dynamics in fMRI. *J. Neurosci. Off. J. Soc. Neurosci.* **34**, 356–362 (2014).
28. Londoño-Ramírez, H. *et al.* Multiplexed Surface Electrode Arrays Based on Metal Oxide Thin-Film Electronics for High-Resolution Cortical Mapping. *Adv. Sci.* **11**, 2308507 (2024).
29. Khodagholy, D. *et al.* NeuroGrid: recording action potentials from the surface of the brain. *Nat. Neurosci.* **18**, 310–315 (2015).
30. Khodagholy, D., Gelinas, J. N. & Buzsáki, G. Learning-enhanced coupling between ripple oscillations in association cortices and hippocampus. *Science* **358**, 369–372 (2017).
31. Tchoe, Y. *et al.* Human brain mapping with multithousand-channel PtNRGrids resolves spatiotemporal dynamics. *Sci. Transl. Med.* **14**, (2022).
32. Chiang, C.-H. *et al.* Flexible, high-resolution thin-film electrodes for human and animal neural research. *J. Neural Eng.* **18**, 045009 (2021).

33. Chiang, C.-H. *et al.* Development of a neural interface for high-definition, long-term recording in rodents and nonhuman primates. *Sci. Transl. Med.* **12**, eaay4682 (2020).

34. Pesaran, B. *et al.* Investigating large-scale brain dynamics using field potential recordings: analysis and interpretation. *Nat. Neurosci.* **21**, 903–919 (2018).

35. Bonaccini Calia, A. *et al.* Full-bandwidth electrophysiology of seizures and epileptiform activity enabled by flexible graphene microtransistor depth neural probes. *Nat. Nanotechnol. 2021 173* **17**, 301–309 (2021).

36. Masvidal-Codina, E. *et al.* High-resolution mapping of infraslow cortical brain activity enabled by graphene microtransistors. *Nat. Mater.* **18**, 280–288 (2019).

37. Garcia-Cortadella, R. *et al.* Graphene active sensor arrays for long-term and wireless mapping of wide frequency band epicortical brain activity. *Nat. Commun.* **12**, 1–17 (2021).

38. Cisneros-Fernandez, J. *et al.* A 1024-Channel 10-Bit 36-µW/ch CMOS ROIC for Multiplexed GFET-Only Sensor Arrays in Brain Mapping. *IEEE Trans. Biomed. Circuits Syst.* **15**, 860–876 (2021).

39. Garcia-Cortadella, R. *et al.* Switchless Multiplexing of Graphene Active Sensor Arrays for Brain Mapping. *Nano Lett.* acs.nanolett.0c00467 (2020) doi:10.1021/acs.nanolett.0c00467.

40. Schaefer, N. *et al.* Multiplexed neural sensor array of graphene solution-gated field-effect transistors. *2D Mater.* **7**, 025046 (2020).

41. Moody, W. J., Futamachi, K. J. & Prince, D. A. Extracellular potassium activity during epileptogenesis. *Exp. Neurol.* **42**, 248–263 (1974).

42. Seigneur, J., Kroeger, D., Nita, D. A. & Amzica, F. Cholinergic Action on Cortical Glial Cells In Vivo. *Cereb. Cortex* **16**, 655–668 (2006).

43. Böhler, C. *et al.* Multilayer Arrays for Neurotechnology Applications (MANTA): Chronically Stable Thin-Film Intracortical Implants. *Adv. Sci.* **10**, 2207576 (2023).

44. Chung, J. E. *et al.* High-Density, Long-Lasting, and Multi-region Electrophysiological Recordings Using Polymer Electrode Arrays. *Neuron* **101**, 21-31.e5 (2019).

45. Over and above frequency: Gamma oscillations as units of neural circuit operations - ScienceDirect. https://www.sciencedirect.com/science/article/pii/S0896627323001307?via%3Dihub.

46. Gervasoni, D. *et al.* Global forebrain dynamics predict rat behavioral states and their transitions. *J. Neurosci. Off. J. Soc. Neurosci.* **24**, 11137–11147 (2004).

47. Sirota, A. *et al.* Entrainment of neocortical neurons and gamma oscillations by the hippocampal theta rhythm. *Neuron* **60**, 683–697 (2008).

48. Taylor, J. A. *et al.* Spontaneous Recurrent Absence Seizure-like Events in Wild-Caught Rats. *J. Neurosci.* **39**, 4829–4841 (2019).

49. Shaw, F.-Z. Is Spontaneous High-Voltage Rhythmic Spike Discharge in Long Evans Rats an Absence-Like Seizure Activity? *J. Neurophysiol.* **91**, 63–77 (2004).

50. Duntley, S. P., Kim, A. H., Silbergeld, D. L. & Miller, J. W. Characterization of the mu rhythm during rapid eye movement sleep. *Clin. Neurophysiol. Off. J. Int. Fed. Clin. Neurophysiol.* **112**, 528–531 (2001).

51. Kozák, G., Földi, T. & Berényi, A. Spike-and-Wave Discharges Are Not Pathological Sleep Spindles, Network-Level Aspects of Age-Dependent Absence Seizure Development in Rats. *eNeuro* **7**, 0253–19.2019 (2020).

52. Reimer, J. *et al.* Pupil fluctuations track rapid changes in adrenergic and cholinergic activity in cortex. *Nat. Commun.* **7**, 13289 (2016).

53. Lecci, S. *et al.* Coordinated infraslow neural and cardiac oscillations mark fragility and offline periods in mammalian sleep. *Sci. Adv.* **3**, e1602026 (2017).

54. Yüzgeç, Ö., Prsa, M., Zimmermann, R. & Huber, D. Pupil Size Coupling to Cortical States Protects the Stability of Deep Sleep via Parasympathetic Modulation. *Curr. Biol.* **28**, 392-400.e3 (2018).

55. Cooper, C. *et al.* Ultraslow serotonin oscillations in the hippocampus delineate substates across NREM and waking. 2024.07.09.602643 Preprint at https://doi.org/10.1101/2024.07.09.602643 (2024).

56. Marshall, L., Mölle, M., Michaelsen, S., Fehm, H. L. & Born, J. Slow Potential Shifts at Sleep—Wake Transitions and Shifts Between NREM and REM Sleep. *Sleep* **19**, 145–151 (1996).

57. Contreras, D. & Steriade, M. Spindle oscillation in cats: the role of corticothalamic feedback in a thalamically generated rhythm. *J. Physiol.* **490**, 159–179 (1996).

58. Helfrich, R. F., Mander, B. A., Jagust, W. J., Knight, R. T. & Walker, M. P. Old Brains Come Uncoupled in Sleep: Slow Wave-Spindle Synchrony, Brain Atrophy, and Forgetting. *Neuron* **97**, 221-230.e4 (2018).

59. Distinction between slow waves and delta waves sheds light to sleep homeostasis and their association to hippocampal sharp waves ripples | bioRxiv. https://www.biorxiv.org/content/10.1101/2022.12.27.522034v1.abstract.

60. Global waves synchronize the brain's functional systems with fluctuating arousal | Science Advances. https://www.science.org/doi/10.1126/sciadv.abf2709.

61. Lu, H. *et al.* Rat brains also have a default mode network. *Proc. Natl. Acad. Sci.* **109**, 3979–3984 (2012).

62. Basu, I. *et al.* Consistent linear and non-linear responses to invasive electrical brain stimulation across individuals and primate species with implanted electrodes. *Brain Stimulat.* **12**, 877–892 (2019).

63. Yang, Y. *et al.* Modelling and prediction of the dynamic responses of large-scale brain networks during direct electrical stimulation. *Nat. Biomed. Eng.* **5**, 324–345 (2021).

64. Ashkan, K., Rogers, P., Bergman, H. & Ughratdar, I. Insights into the mechanisms of deep brain stimulation. *Nat. Rev. Neurol.* **13**, 548–554 (2017).

65. Cherian, R. & Kanaga, E. G. Theoretical and methodological analysis of EEG based seizure detection and prediction: An exhaustive review. *J. Neurosci. Methods* **369**, 109483 (2022).

66. Maingret, N., Girardeau, G., Todorova, R., Goutierre, M. & Zugaro, M. Hippocampo-cortical coupling mediates memory consolidation during sleep. *Nat. Neurosci.* **19**, 959–964 (2016).

67. Sirota, A., Csicsvari, J., Buhl, D. & Buzsáki, G. Communication between neocortex and hippocampus during sleep in rodents. *Proc. Natl. Acad. Sci. U. S. A.* **100**, 2065–2069 (2003).

68. Kim, J., Gulati, T. & Ganguly, K. Competing Roles of Slow-Oscillations and Delta-Waves in Memory Consolidation Versus Forgetting. *Cell* **179**, 514-526.e13 (2019).

69. Kim, D., Hwang, E., Lee, M., Sung, H. & Choi, J. H. Characterization of Topographically Specific Sleep Spindles in Mice. *Sleep* **38**, 85.

70. Andrillon, T. *et al.* Sleep Spindles in Humans: Insights from Intracranial EEG and Unit Recordings. *J. Neurosci.* **31**, 17821–17834 (2011).

71. Cox, R., Schapiro, A. C., Manoach, D. S. & Stickgold, R. Individual Differences in Frequency and Topography of Slow and Fast Sleep Spindles. *Front. Hum. Neurosci.* **11**, 433 (2017).

72. Zygierewicz, J. High resolution study of sleep spindles. *Clin. Neurophysiol.* **110**, 2136–2147 (1999).

73. Blanco-Duque, C. *et al.* Oscillatory-Quality of sleep spindles links brain state with sleep regulation and function. *Sci. Adv.* **10**, eadn6247 (2024).

74. Sirota, A. & Buzsáki, G. Interaction between neocortical and hippocampal networks via slow oscillations. *Thalamus Relat. Syst.* **3**, 245 (2005).

75. Massimini, M., Huber, R., Ferrarelli, F., Hill, S. & Tononi, G. The Sleep Slow Oscillation as a Traveling Wave. *J. Neurosci.* **24**, 6862–6870 (2004).

76. Vyazovskiy, V. V. *et al.* Local sleep in awake rats. *Nature* **472**, 443–447 (2011).

77. Rasmussen, R., Jensen, M. H. & Heltberg, M. L. Chaotic Dynamics Mediate Brain State Transitions, Driven by Changes in Extracellular Ion Concentrations. *Cell Syst.* **5**, 591-603.e4 (2017).

78. Sakata, S. & Harris, K. D. Laminar Structure of Spontaneous and Sensory-Evoked Population Activity in Auditory Cortex. *Neuron* **64**, 404–418 (2009).

79. Kandel, A. & Buzsáki, G. Cellular–Synaptic Generation of Sleep Spindles, Spike-and-Wave Discharges, and Evoked Thalamocortical Responses in the Neocortex of the Rat. *J. Neurosci.* **17**, 6783–6797 (1997).

80. Krishnan, G. P., Filatov, G., Shilnikov, A. & Bazhenov, M. Electrogenic properties of the Na^+/K^+ ATPase control transitions between normal and pathological brain states. *J. Neurophysiol.* **113**, 3356–3374 (2015).

81. Watson, B. O., Levenstein, D., Greene, J. P., Gelinas, J. N. & Buzsáki, G. Network Homeostasis and State Dynamics of Neocortical Sleep. *Neuron* **90**, 839–852 (2016).

82. Herreras, O. Local field potentials: Myths and misunderstandings. *Front. Neural Circuits* **10**, 101 (2016).

83. Dietz, A. G. *et al.* Local extracellular K+ in cortex regulates norepinephrine levels, network state, and behavioral output. *Proc. Natl. Acad. Sci.* **120**, e2305071120 (2023).

84. Tsai, C.-J. *et al.* Cerebral capillary blood flow upsurge during REM sleep is mediated by A2a receptors. *Cell Rep.* **36**, 109558 (2021).

85. Bangash, M. F. *et al.* Cerebrovascular Response to Arousal from NREM and REM Sleep. *Sleep* **31**, 321 (2008).

86. Rubehn, B. & Stieglitz, T. In vitro evaluation of the long-term stability of polyimide as a material for neural implants. *Biomaterials* **31**, 3449–3458 (2010).

87. Hassler, C., Boretius, T. & Stieglitz, T. Polymers for neural implants. *J. Polym. Sci. Part B Polym. Phys.* **49**, 18–33 (2011).

88. Schaefer, N. *et al.* Improved metal-graphene contacts for low-noise, high-density microtransistor arrays for neural sensing. *Carbon* **161**, 647–655 (2020).

89. Lu, H. *et al.* SU8-based micro neural probe for enhanced chronic in-vivo recording of spike signals from regenerated axons. in *Proceedings of IEEE Sensors* 66–69 (2006). doi:10.1109/ICSENS.2007.355719.

90. Márton, G. *et al.* A multimodal, SU-8 - Platinum - Polyimide microelectrode array for chronic in vivo neurophysiology. *PLoS ONE* **10**, (2015).

91. Felix, S. H. *et al.* Insertion of Flexible Neural Probes Using Rigid Stiffeners Attached with Biodissolvable Adhesive. *J. Vis. Exp. JoVE* 50609 (2013) doi:10.3791/50609.

92. Garcia-Cortadella, R. *et al.* Distortion-Free Sensing of Neural Activity Using Graphene Transistors. *Small* **16**, 1906640 (2020).

93. Schmitzer-Torbert, N. & Redish, A. D. Neuronal Activity in the Rodent Dorsal Striatum in Sequential Navigation: Separation of Spatial and Reward Responses on the Multiple T Task. *J. Neurophysiol.* **91**, 2259–2272 (2004).

94. Craig E. Tenke, J. K. Optimizing PCA Methodology for ERP Component Identification and Measurement: Theoretical Rationale and Empirical Evaluation. *Clin. Neurophysiol.* (2003).

95. Benjamini, Y. & Hochberg, Y. Controlling the False Discovery Rate: A Practical and Powerful Approach to Multiple Testing. *J. R. Stat. Soc. Ser. B Methodol.* **57**, 289–300 (1995).

Acknowledgments

This work has been funded by the European Union's Horizon 2020 research and innovation program under Grant Agreement No. 732032 (BrainCom), Grant Agreement No. 881603 (GrapheneCore3). Research at the LMU was supported by the Bundesministerium für Bildung und Forschung [grant number 01GQ0440]. ICN2 is supported by the Severo Ochoa Centres of Excellence programme, funded by the Spanish Research Agency (AEI, grant no. SEV-2017–0706), and by the CERCA Programme/Generalitat de Catalunya. RGC received funding from the Alexander von Humboldt foundation and the Marie Curie individual fellowship program. This work has made use of the Spanish ICTS Network MICRONANOFABS, partially supported by MICINN and the ICTS 'NANBIOSIS', more specifically by the Micro-NanoTechnology Unit of the CIBER in Bioengineering, Biomaterials and Nanomedicine (CIBER-BBN) at the IMB-CNM. We also acknowledge funding from the Generalitat de Catalunya (2017 SGR 1426), and the 2DTecBio project (FIS2017-85787-R) funded by the Ministerio de Ciencia, Innovación y Universidades of Spain, the Agencia Estatal de Investigación (AEI) and the Fondo Europeo de Desarrollo Regional (FEDER/UE). Part of this work was co-funded by the European Regional Development Funds (ERDF) allocated to the Programa operatiu FEDER de Catalunya 2014–2020, with the support of the Secretaria d'Universitats i Recerca of the Departament d'Empresa i Coneixement of the Generalitat de Catalunya for emerging technology clusters devoted to the valorization and transfer of research results (GraphCAT 001-P-001702).

Author contributions

RGC contributed to the conceptual development of graphene recording systems, fabrication and characterization of graphene probes, development and execution of surgical procedures, acquisition of electrophysiological recordings, data analysis and manuscript preparation. JCF designed and characterised the ASIC and developed the headstage hardware, data communication protocols and data acquisition software. GS developed the techniques for the chronic implantation of large-scale probes. AS contributed to the factor analysis of sleep spindles. AU contributed to the data pre-processing and analysis of infra-slow dynamics. NS contributed to the conceptual design of graphene recording systems and fabrication of graphene probes. JA contributed to the development of the discrete electronics system for the operation of graphene probes. EMC contributed to the conceptual development of the technology. EDC contributed to the development of the graphene flexible electronics. RM development of electronics for ASIC headstage. JP and MK implemented the firmware for digital data communication. HL developed the software for recording and analysis. CJ and JM tested and validated the operation of the ASIC headstage. XI contributed to the design and fabrication of graphene probes. FSG led the team for the design of the ASIC and headstage. AGB and JAG coordinated the development of graphene recording systems. AS contributed to the conceptual development of the technologies and experiments. Supervised the electrophysiological recordings, data analysis and manuscript preparation.